Article:
Zhang, Y., Guan, X. orcid.org/0009-0005-9594-9335, Gu, J. orcid.org/0000-0001-7735-4702 et al. (7 more authors) (2025) Achieving ultrahigh elastocaloric cycling stability in Ni-Mn-Sn-based alloys by microstructure engineering. Acta Materialia, 301. 121512. ISSN: 1359-6454

https://doi.org/10.1016/j.actamat.2025.121512

Achieving ultrahigh elastocaloric cycling stability in Ni-Mn-Sn-based alloys by microstructure engineering

Yu Zhang[1,2], Xu Guan[1], Jianglong Gu[3], Keliang Guo[1], Jing Bai[1,2,*], Jing Yang[2], Qingshuang Ma[2], Qiuzhi Gao[2], Nicola Morley[4], Liang Zuo[1]

[1]Key Laboratory for Anisotropy and Texture of Materials (Ministry of Education), School of Material Science and Engineering, Northeastern University, Shenyang 110819, China

[2]Key Laboratory of Dielectric and Electrolyte Functional Material Hebei Province, School of Resources and Materials, Northeastern University at Qinhuangdao, Qinhuangdao 066004, PR China

[3]State Key Laboratory of Metastable Materials Science and Technology, Yanshan University, Qinhuangdao 066004, China

[4]Department of Material Science and Engineering, University of Sheffield, Sheffield, S1 3JD, UK

*Corresponding author: Jing Bai: baijing@neuq.edu.cn

Abstract

Developing superelastic shape memory alloys that integrate a large elastocaloric response with excellent cyclic stability is crucial for advancing solid-state elastocaloric refrigeration technology. In this study, first-principles calculations were utilized to clarify the preferential occupation of doped B atoms. The mechanism by which B alloying enhances the mechanical properties was investigated through elastic constants and differential charge density analysis. We further proposed an effective microstructure regulation strategy of suction casting combined with B alloying synergistically refines grains and introduces non-transforming secondary phases. This approach significantly improves both the mechanical performance and the cyclic stability of the elastocaloric effect in Ni-Mn-Sn alloys. A fine-grained $(Ni_{43.5}Mn_{46}Sn_{10.5})_{98.5}B_{1.5}$ alloy, featuring Mn_2B precipitates at grain boundaries, achieved a large adiabatic temperature variation ($|\triangle T_{ad}|$) of 9.8 K upon unloading from a 3% compressive strain at 298 K. This excellent superelasticity and elastocaloric refrigeration performance were sustained across a wide temperature range from 288 K to 368 K. Moreover, the alloy exhibited exceptional elastocaloric stability with minimal degradation after 10^5 cycles under 600 MPa compressive stress, maintaining $|\Delta T_{ad}|$ from 9.8 K initially to 9.2 K after 10^5 cycles, outperforming most reported Ni-Mn-base and Ni-Fe-based ferromagnetic shape memory alloys.

Keywords: Ni-Mn-Sn-based alloy; First-principles calculations; Elastocaloric effect; Superelasticity; Cyclic stability

1. Introduction

Refrigeration systems such as air conditioners and refrigerators are indispensable in modern life, and are widely used in food storage, logistics transportation, and biotechnology. However, conventional vapor compression technology raises concerns due to its high energy consumption and environmental risks associated with volatile liquid refrigerant emissions[1]. Solid-state elastocaloric refrigeration, based on the elastocaloric effect (eCE), offers an eco-friendly, efficient, and energy-saving alternative[2]. Among the various alloys currently under investigation, Ni-Mn-X (X = Ga, In, Sn, Sb) based Heusler-type ferromagnetic shape memory alloys (FMSMAs) stand out for their ability to exhibit an elastocaloric response through the utilization of released and absorbed latent heat during stress-induced martensitic transformation (MT). Notably, Ni-Mn-Sn-based FMSMAs offer larger transformation entropy changes and lower costs compared to Ni-Mn-Ga and Ni-Mn-In alloys, demonstrating considerable application potential.

Polycrystalline Ni-Mn-Sn alloys face significant challenges in refrigeration technology applications due to both functional fatigue (e.g., degradation of eCE and its reversibility) and structural fatigue (e.g., material integrity damage) under cyclic mechanical loading[3-5]. In contrast, Ni-Ti-based shape memory alloys exhibit excellent fatigue resistance, primarily attributed to grain refinement achieved through processing methods such as cold rolling and high-pressure torsion[6-10]. For example, NiTi alloys with a grain size of 35 nm exhibited a $|\triangle T_{ad}|$ of 18.8 K after 10^4 cycles[9], while NiTi microwires with an average grain size of 100 nm demonstrated a fatigue life exceeding 2×10^7 cycles under an applied stress of 800 MPa, maintaining a $|\triangle T_{ad}|$ of 8 K[10]. However, the severe plastic deformation techniques necessary for such grain refinement are challenging to implement effectively in polycrystalline Ni-Mn-Sn alloys. Beyond the predominant *p-d* covalent hybridization, lattice dynamics during MT play a critical role in poor cyclic stability. The shearing of the {110} plane along the $<\bar{1}10>$ direction is the only activated deformation system capable of accommodating external strain[11]. This results in inevitable strain discontinuities among grains with different crystallographic orientations. Due to weak grain boundary cohesion, the localized stress decomposed from strain discontinuity can exceed the fracture strength, ultimately driving crack nucleation and propagation along grain boundaries.

To address these challenges, recent studies have focused on B alloying as an effective strategy

for grain refinement and enhanced grain boundary cohesion, thereby improving mechanical properties and elastocaloric cyclic stability[12-14]. The B alloying promotes the formation of secondary phases, which provide more nucleation sites for stress-induced MT. These nucleation sites facilitate the formation and subsequent coalescence of the martensites during stress loading process, which suppresses the long-range movement of phase interfaces, thereby reducing frictional resistance and minimizing dissipative energy.[15]. However, grain refinement is effective only within a specific range of B content. Excessive B addition not only fails to refine the grain size but also leads to excessive secondary-phase precipitation, which can suppress MT. Additionally, the underlying physical mechanisms behind the improvement of mechanical properties through B alloying remain insufficiently explored.

This work proposes a microstructure engineering approach that combines suction casting, which refines grains through rapid solidification, and B alloying, which both refines grains and introduces secondary phases, resulting in a synergistic effect that improves the mechanical properties and cyclic stability of eCE. To establish the role of B alloying, we first employed the first-principles calculations to determine the preferential occupation of B atoms and their influence on mechanical properties. Based on these insights, $(Ni_{43.5}Mn_{46}Sn_{10.5})_{100-x}B_x$ (x=0, 0.5, 1, 1.5, and 2 at.%) alloys were prepared via suction casting, followed by annealing under controlled cooling rates to ensure uniform microstructure and avoid grain coarsening. The effects of microstructure regulation on mechanical properties and stress-induced MT behavior were systematically investigated. This study revealed that the $(Ni_{43.5}Mn_{46}Sn_{10.5})_{98.5}B_{1.5}$ alloy with an average grain size of ~40 μm, exhibits the highest fracture compressive strength (1.2 GPa) and strain (7.62%). Additionally, this alloy demonstrates an exceptionally stable eCE with negligible degradation over 10^5 cycles under a compressive stress of 600 MPa, showing a cooling $|\triangle T_{ad}|$ of 9.8 K initially and 9.2 K after 10^5 cycles, outperforming most reported Ni-Mn-based and Ni-Fe-based FMSMAs. Thus, synergistic regulation of microstructure through alloying, optimized preparation process, and controlled annealing represents an effective strategy for realizing large eCE with exceptional cycling stability.

2. Computational and experimental details

2.1 Computational methods

All calculations utilized spin-polarized density functional theory (DFT) as implemented in the

Vienna Ab Initio Simulation Package (VASP)[16,17]. The interaction between ions and electrons was described using the projector-augmented wave (PAW) pseudopotential method. For the exchange-correlation functional, the Perdew-Burke-Ernzerhof (PBE) generalized gradient approximation (GGA) approach was employed[18-20]. Valence electron configurations used for Ni, Mn, Sn, and B were $3d^8 4s^2$, $3d^6 4s^1$, $4d^{10} 5s^2 5p^2$, and $2s^2 2p^1$ respectively. The structural relaxation was carried out with a plane-wave cutoff energy of 414 eV. The convergence criteria for total energy and force were set to 10^{-4} eV and 0.02 eV/Å, respectively. The elastic constants C_{ij} were calculated using the strain-energy approach[21].

2.2 Experimental details

Polycrystalline $(Ni_{43.5}Mn_{46}Sn_{10.5})_{100-x}B_x$ (x=0, 0.5, 1, 1.5, and 2 at.%, termed as B_0, $B_{0.5}$, B_1, $B_{1.5}$, and B_2, respectively) alloys were prepared by repeated arc melting and then suction casting into a copper mold with internal dimensions of 7 mm × 20 mm × 60 mm under the high-purity Ar atmosphere using high purity elements of Ni, Mn, Sn and B (>99.98 wt%). An additional 1 wt% Mn was pre-added to compensate for Mn loss due to evaporation during melting. The actual chemical compositions of the prepared alloys were measured and are provided in Table S1 of the Supplementary Materials. The suction-cast alloys were then sealed into vacuum quartz tubes and annealed at 1173 K for 2 hours to homogenize the microstructure and chemical composition, followed by air-cooled. To compare the effect of different cooling rates during annealing on the performance, additional experiments involving water cooling and furnace cooling experiments were conducted on the $(Ni_{43.5}Mn_{46}Sn_{10.5})_{98.5}B_{1.5}$ alloy. For clarity, unless otherwise specified, all alloys discussed in the following text refer to those prepared by suction casting and air cooling during annealing.

The microstructure was characterized using a scanning electron microscope (SEM, JEOL JSM-7001F) equipped with an Oxford electron backscatter diffraction (EBSD) attachment. The crystal structure was analyzed using X-ray diffraction (XRD, Rigaku Smartlab) with Cu-Kα radiation. To determine the forward and reverse martensitic transformation temperatures (M_s, M_f, A_s, and A_f), the temperature dependence of heat flow was monitored using a differential scanning calorimeter (DSC, TA Instruments Discovery DSC25) at a constant heating/cooling rate of 10 K/min. The alloy compositions were determined using a wavelength-dispersive spectrometer (WDS) on a field emission electron probe microanalyzer (JEOL JXA-8530F). Mechanical and elastocaloric properties under compression were studied using a universal testing machine (Shimadzu AG-XPlus 50 kN),

where the load was applied along the longer edge of the 3 × 4 × 5 mm^3 samples (the solidification direction of suction-casting), as shown in Supplementary Fig. S1. Displacement data during the compression tests were recorded using a linear gauge (Mitutoyo LG100-0110) with a resolution of 0.1 μm. Mechanical cycling test was carried out on a fatigue machine (Shimadzu SCL-20 kN) under sinusoidal cyclic compression with a maximum stress of 600 MPa and a loading frequency of 20 Hz. The adiabatic temperature variation was recorded by a data acquisition unit that monitored signals using a Pt100 resistance temperature detector clamped to the center of the sample surface, with a sampling frequency of 10 Hz. For accurate measure $|\triangle T_{ad}|$ during reverse martensitic transformation, the alloy was loaded to the specified strain, held for 15 seconds to stabilize at ambient temperature, and then unloaded.

3. Results and discussion

3.1 Preferred occupation of B and its effect on mechanical properties

To investigate the preferred site occupation of B atoms in Ni-Mn-Sn alloys, the $Ni_2Mn_{1.5}Sn_{0.5}$ alloy was selected as the matrix alloy, mainly because previous studies revealed martensitic transformation occurs when $x \geq 0.5$ in $Ni_2Mn_{1+x}Sn_{1-x}$ alloys[22], and its high structural symmetry helps to enhance computational efficiency. The austenite of the $Ni_2Mn_{1.5}Sn_{0.5}$ alloy exhibits a high-symmetry Cu_2AlMn-type $L2_1$ structure. Although the $L2_1$ structure is typically classified as face-centered cubic (FCC) based on crystallographic symmetry, the stacking arrangement conforms to the characteristics of a body-centered cubic (BCC) crystal[23]. Since the interstitial positions in a crystal are determined by the arrangement of atoms, the number and character of the interstitial sites in $Ni_2Mn_{1.5}Sn_{0.5}$ follow the features of the BCC crystal.

Furthermore, small-radius B atoms doped into the alloy preferentially occupy interstitial lattice sites. In a BCC crystal, two types of interstitial sites exist, i.e., smaller octahedral interstices ($r_o \approx 0.155 r_a$, r_o represents the radius of the octahedral interstices) and larger tetrahedral interstices ($r_T \approx 0.291 r_a$, r_T represents the radius of the tetrahedral interstices), where r_a represents the average atomic radius of the elements forming the interstice. Based on the atomic environment of the $Ni_2Mn_{1.5}Sn_{0.5}$ alloy, three distinct types of octahedral interstices are formed: O-I, surrounded by 2 Ni, 2 Mn_{Mn} (normal Mn atoms), and 2 Mn_{Sn} (Mn atoms occupy the Sn sublattices) atoms (Fig. 1(a_1)-(a_2)); O-II, surrounded by 2 Ni, 2 Mn_{Mn}, 1 Mn_{Sn}, and 1 Sn atom (Fig. 1(b_1)-(b_2)); and O-III, surrounded by

4 Ni, 1 Mn_{Mn}, and 1 Mn_{Sn} atom (Fig. 1(c_1)-(c_2)). Additionally, two types of tetrahedral interstices are present: T-I, surrounded by 2 Ni, 1 Mn_{Mn}, and 1 Sn atom (Fig. 1(d_1)-(d_2)); and T-II, surrounded by 2 Ni, 1 Mn_{Mn}, and 1 Mn_{Sn} atom (Fig. 1(e_1)-(e_2)).

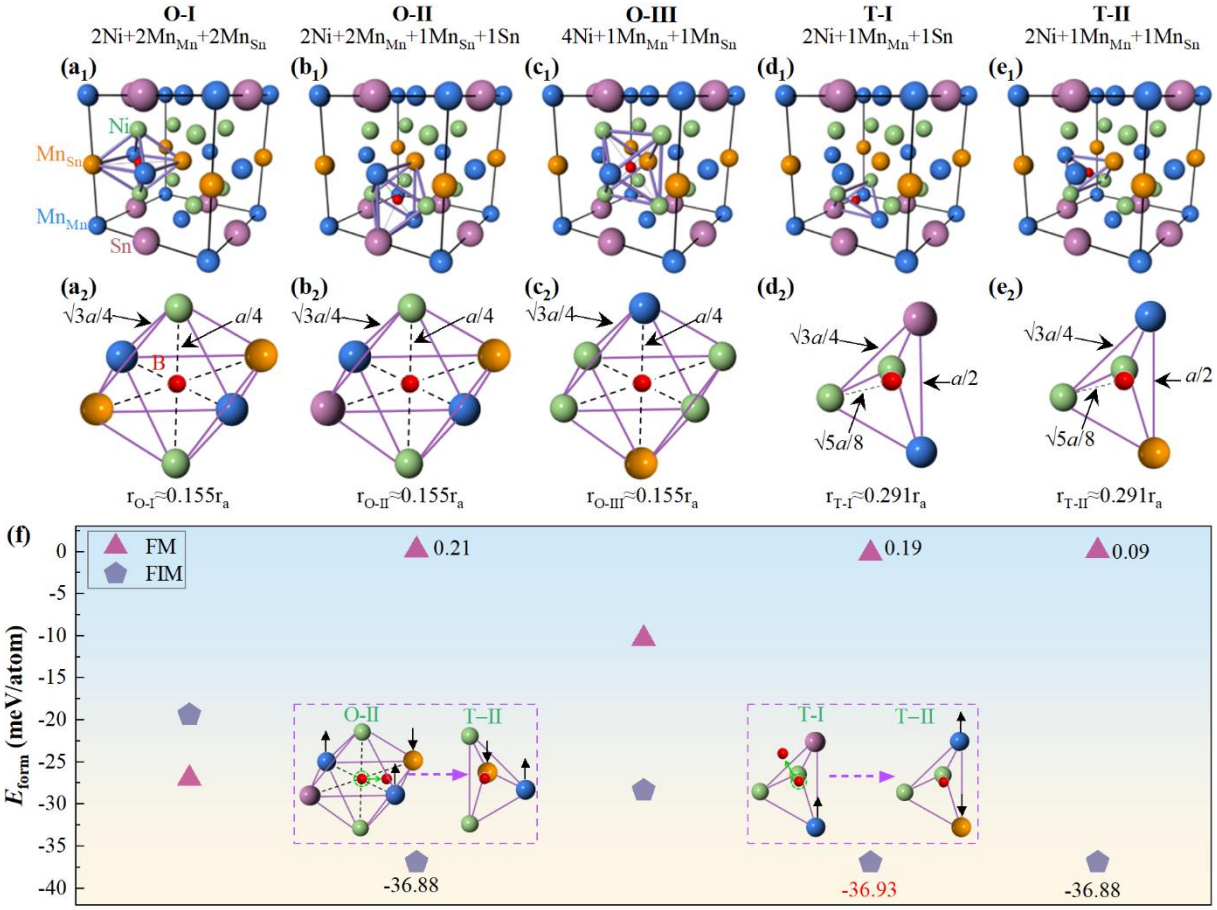

Fig. 1. Diagram of (a_1)-(a_2) octahedral interstice of O-I, (b_1)-(b_2) octahedral interstice of O-II, (c_1)-(c_2) octahedral interstice of O-III, (d_1)-(d_2) tetragonal interstice of T-I, and (e_1)-(e_2) tetragonal interstice of T-II for $(Ni_2Mn_{1.5}Sn_{0.5})_{0.94}B_{0.06}$ alloy. (f) Formation energies E_{form} of various occupation models for $(Ni_2Mn_{1.5}Sn_{0.5})_{0.94}B_{0.06}$ alloy (arrows represent the spin direction of the magnetic moment of the Mn atom).

The optimal site occupancy of B atoms can be determined by the formation energy (E_{form}), calculated as: E_{form}=1000*(E_{total}-$N_{Ni}E_{Ni}$-$N_{Mn}E_{Mn}$-$N_{Sn}E_{Sn}$-N_BE_B)/N_{total}, where E_{total} represents the total ground-state energy of compound, N_X (X = Ni, Mn, Sn, B) is the atomic number of element X, and E_X denotes the ground-state energy per atom of each pure element X in its reference bulk state. As shown in Fig. 1(f), the formation energies of the FIM state are lower than those of the FM state for all interstices except the O-I, where the FM state has a lower formation energy than the FIM state. During the structural optimization process, B atoms spontaneously migrate from the O-II and T-I interstitial sites to the T-II type in the FIM state, indicating that the T-II interstice in the FIM state is highly stable. Furthermore, the formation energy of the FIM state in the T-II interstice is significantly

lower than that of the O-I and O-III stable magnetic configurations. In conclusion, the FIM state in the T-II interstice has the lowest formation energy, indicating that this configuration is the most stable. This is likely due to the high symmetry of the interstice, which consists of 2Ni and 2Mn atoms, contributing to its enhanced structural stability.

The superior mechanical properties of Ni-Mn-based Heusler alloys are crucial for their practical applications. Typically, the inherent brittleness or toughness can be evaluated using parameters such as the bulk-to-shear modulus ratio (B/G, known as Pugh's ratio), Cauchy pressure (P_c), and Poisson's ratio (v). The validity of these indicators has been well established in Ni-Mn-based Heusler alloys[24,25]. Since the experimental measured shear modulus (G) of many Ni-Mn-based Heusler alloys closely approximates Voigt shear modulus (G_v), it is reasonable to assume $G \approx G_v$[26,27]. When $B/G_v > 1.75$, the material exhibits good ductility, with higher values indicating improved toughness[28]. A positive P_c suggests strong metallic bonding and good toughness[29]. Poisson's ratio v is also used to describe the lattice stability and plasticity, when $v > 0.33$, the material shows good ductility, and higher v value corresponds to enhanced plasticity[30,31]. Fig. 2 shows the B/G_v, P_c, and v for the $Ni_2Mn_{1.5}Sn_{0.5}$ and $(Ni_2Mn_{1.5}Sn_{0.5})_{0.94}B_{0.06}$ alloys obtained through calculations. Compared to the ternary alloy, the B/G_v value of the B-doped alloy significantly increases to 4.25, with the P_c nearly doubling and the v rising to 0.39. Notably, the fracture strength of intermetallic, such as the Ni-Mn-based alloys investigated in this study, is predominantly governed by the brittleness rather the their inherent strength[32]. So, these theoretical predictions suggest that the mechanical properties of Ni-Mn-Sn-B alloys are expected to outperform those of their Ni-Mn-Sn counterparts.

The ductility and toughness of materials are fundamentally determined by their electronic structure. To elucidate the underlying mechanism by which doping B interstitial atoms significantly enhances the ductility of the alloy, we calculated the differential charge density maps for the $Ni_2Mn_{1.5}Sn_{0.5}$ and $(Ni_2Mn_{1.5}Sn_{0.5})_{0.94}B_{0.06}$ alloys on the (020) plane, as shown in Fig. 2. The introduction of B atoms into the tetrahedral interstitial sites establishes new Mn-B and Sn-B interactions. Simultaneously, the Mn-Sn interactions are weakened, leading to a reduction in the overall bonding strength between atoms. Furthermore, a pronounced Mn_{Sn}-Mn electronic overlap region is observed, which can be attributed to local distortions caused by B doping. This distortion decreases the interatomic distance from 2.96 Å (in the $Ni_2Mn_{1.5}Sn_{0.5}$ alloy) to 2.12 Å, facilitating atomic hybridization and the formation of *d-d* bonds, analogous to metallic bonds. Compared to *p-d*

bonds, *d-d* bonds exhibit stronger interactions with minimal directionality, thereby promoting microstructural rearrangement under external stress and enhancing plastic deformation capability.

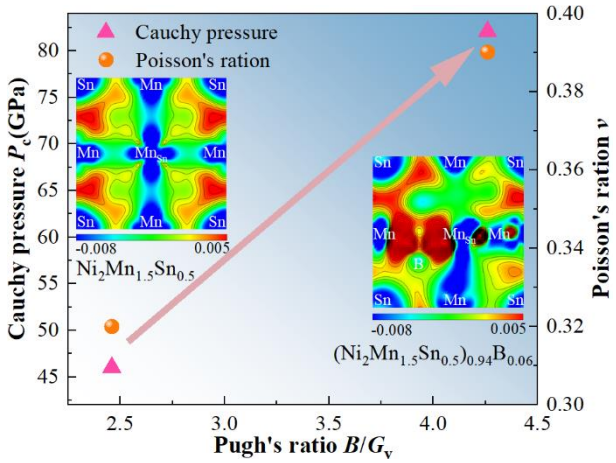

Fig. 2. Comparison of Pugh's ratio, P_c, and ν values, along with differential charge density maps on (020) plane for $Ni_2Mn_{1.5}Sn_{0.5}$ and $(Ni_2Mn_{1.5}Sn_{0.5})_{0.94}B_{0.06}$ alloys.

3.2 Microstructure and mechanical properties

Fig. 3 presents the microstructure of the $(Ni_{43.5}Mn_{46}Sn_{10.5})_{100-x}B_x$ alloys. To investigate the effect of B doping, backscattered electron (BSE) images of these alloys were examined, as shown in Fig. 3(a)-(d). The results reveal that an appropriate amount of B doping significantly promotes grain refinement. In the B-free alloy (B_0), the average grain size is approximately 199.7 μm (Fig. 3(a)). At x=0.5, the grains are notably refined, reducing to ~95.5 μm (Fig. 3(b)). As the B content increases to x=1.5, the grain size further decreases to around 40 μm (Fig. 3(c)). However, increasing B content (x=2) does not lead to further grain refinement; instead, the grain size slightly increases to about 44.5 μm (Fig. 3(d)).

Furthermore, B doping induces the formation of a secondary phase. With an appropriate amount of B doping, these secondary phases are predominantly distributed along grain boundaries, with a few dispersed within the grains (Fig. 3(b) and the high-magnification image of a local region in Fig. 3(c)). At x=2, the secondary phases become more abundant and are distributed both along the grain boundaries and within the grains. Quantitative analysis using Image-Pro Plus reveals that the area fractions of the secondary phase for the x=0.5, x=1.5, and x=2 alloys to be 1.2%, 4.1%, and 4.8%, respectively. Notably, in the x=1.5 alloy, approximately 3.9% of the total 4.1% secondary phase area fraction is located along grain boundaries, while only a small portion is found within the grains. In contrast, for the x=2 alloy, although the total secondary phase fraction is slightly higher (4.8%), only 1.6% of this is distributed along grain boundaries, with the majority precipitating within the grains.

These observations indicate that grain refinement depends not only on the total area fraction of the secondary phase but also critically on its spatial distribution. Secondary phases precipitated along grain boundaries effectively hinder grain boundary migration via the classical Zener pinning effect[33], thereby suppressing grain growth and coarsening, and leading to refined grain structures. Conversely, when secondary phases predominantly precipitate within the grains, their ability to pin grain boundaries is significantly diminished, resulting in no further grain refinement and even a slight increase in grain size.

In summary, an appropriate B doping (around 0~1.5 at.%) promotes the precipitation of secondary phases along grain boundaries, which effectively hinder grain boundary migration, thereby restricting grain growth and coarsening, leading to refined grain structures; however, at higher B content (x=2), secondary phases preferentially precipitate within the grains, reducing their pinning efficiency and limiting further grain refinement. The lattice structure and composition of the secondary phase will be discussed in subsequent analyses.

Based on EBSD measurements, the austenite in the suction-cast $B_{1.5}$ alloy exhibits fine equiaxed grains (Fig. 3(e)), whereas the austenite in the arc-melted $B_{1.5}$ alloy shows significantly coarser grains (Fig. 3(f)). This comparison highlights the role of rapid solidification during suction casting in increasing nucleation sites while suppressing grain growth, thereby resulting in a fine-grained structure. Such grain refinement is expected to significantly enhance the alloy's mechanical properties. Although processing techniques such as melt spinning, magnetron sputtering, and cold rolling can produce submicron or even nanometer-sized grains, their applicability is often limited. The constraints arise from the restricted sample thickness, which hinders large-scale applications, and the inherent grain boundary weakness of Heusler alloys[7,34-36].

The effects of different cooling rates during annealing on the microstructure were investigated while maintaining a consistent composition and preparation method. The suction-cast $B_{1.5}$ alloy was additionally subjected to water cooling and furnace cooling, and the results were compared with those of the air-cooled sample. Statistical analysis of the orientation maps reveals that the grain size of the water-cooled sample (Fig. 3(g)) is similar to that of the air-cooled sample (Fig. 3(h)), measuring 36.9 and 39.3 μm, respectively, whereas the grain size of the furnace-cooled sample (Fig. 3(i)) is about 68.5 μm, nearly twice that of the other two.

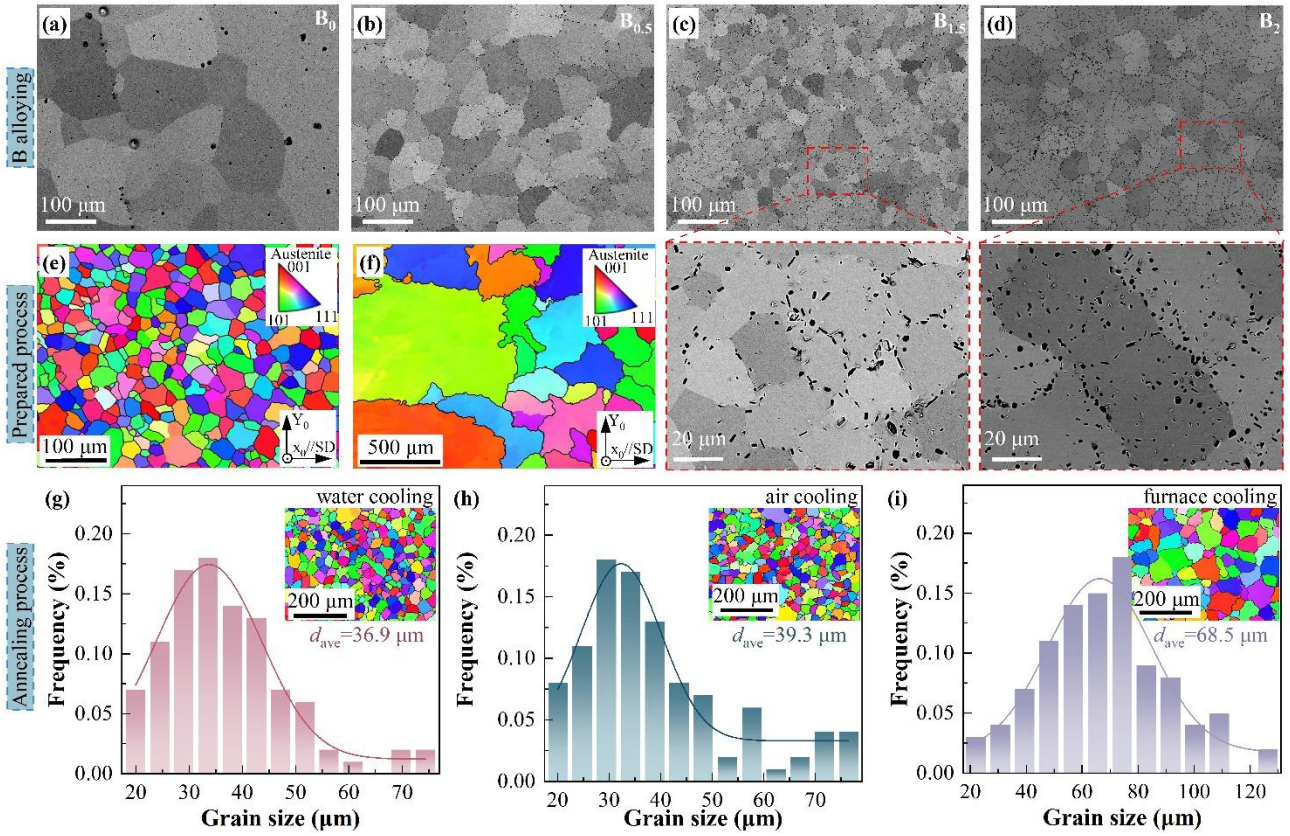

Fig. 3. BSE micrographs of suction-cast $(Ni_{43.5}Mn_{46}Sn_{10.5})_{100-x}B_x$ alloys with (a)x=0, (b)x=0.5, (c)x=1.5, and (d)x=2; IPF-X (inverse pole figure X-direction) maps of (e) suction-cast and (f) arc-melted x=1.5 alloy showing grain sizes along solidification direction (SD) (All alloys in (a)-(f) at air cooling during annealing); Grain size distribution of suction-cast x=1.5 alloy at different cooling rates during annealing: (g) water cooling, (h) air cooling, and (i) furnace cooling.

To clarify the composition and crystallographic characteristics of the secondary phase, EBSD characterization was conducted on the $B_{1.5}$ alloy (suction-casting and air-cooling), as shown in Fig. 4. Fig. 4(b) is the composition diagram corresponding to Fig. 4(a), which reveals the distribution of elements, showing significant segregation of Mn and B in the secondary phase. Further WDS analysis provided the precise composition of the secondary phase: Ni = 1.29 at.% (4.88%), Mn = 66.99 at.% (0.4%), Sn = 0.26 at.% (4.55%), and B = 31.46 at.% (3.14%) (the values in brackets represent errors), with a Mn-to-B atomic ratio of approximately 2:1. To further determine the crystallographic features of the secondary phase, using the structural information of tetragonal Mn_2B as a reference, Fig. 4(c_1) and (c_2) show the overlapped measured and simulated electron backscattered diffraction (*i.e.*, *Kikuchi*) patterns for austenite and secondary phase, respectively. A good match between the measured and indexed *Kikuchi* patterns indicates that the crystal structure of the secondary phase is consistent with the tetragonal Mn_2B (Fig. (d_2)), confirming its identification as Mn_2B. Researchers also observed the

Mn_2B phase in the Ni-Mn-Sn-B alloy through XRD measurement[37,38]. The room temperature XRD patterns of B_0 and $B_{1.5}$ are shown in Supplementary Fig. S2. Comparison reveals that adding B does introduce the Mn_2B phase.

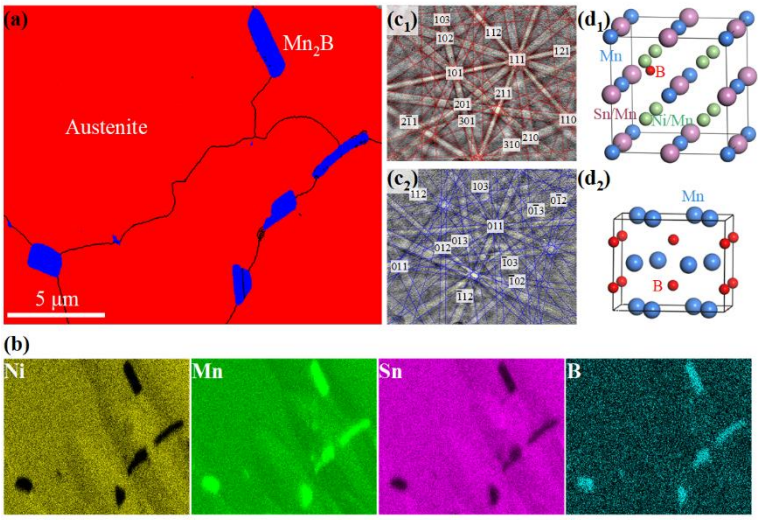

Fig. 4. Microstructure of $(Ni_{43.5}Mn_{46}Sn_{10.5})_{98.5}B_{1.5}$ alloy (suction-casting and air-cooling): (a) Phase contrast map, (b) Composition maps of Ni, Mn, Sn, and B were measured in the same region of (a), Indexed *Kikuchi* patterns of (c_1) austenite and (c_2) secondary phase, Crystal structure of (d_1) austenite and (d_2) secondary phase.

Achieving a notable elastocaloric effect requires materials with excellent mechanical properties capable of withstanding sufficient uniaxial stress to drive phase transformation. Therefore, compressive tests were conducted on the $(Ni_{43.5}Mn_{46}Sn_{10.5})_{100-x}B_x$ (x=0, 0.5, 1, 1.5, 2) alloys to evaluate their mechanical properties, with compressive stress-strain curves measured at 298 K with a strain rate of $1.67\times10^{-4}s^{-1}$. Stress-induced martensitic transformation was observed in all alloys. As shown in Fig. 5(a), under identical prepared (suction-cast) and annealing (air cooling) conditions, both fracture compressive strength and strain initially increased and then decreased with the increase in B content. Notably, the $B_{1.5}$ alloy achieves a fracture compressive strength of 1.2 GPa and a fracture strain of 7.62%, significantly exceeding those of the B_0 alloy. This suggests that appropriate B alloying effectively enhances the alloy's mechanical properties, allowing it to withstand higher stress and thus improve its elastocaloric performance. Supplementary Fig. S3 presents the fracture morphologies of the B_0 and $B_{1.5}$ alloys at room temperature. The B_0 alloy predominantly exhibited intergranular fracture, while the $B_{1.5}$ alloy displayed many river-like patterns formed by uneven cleavage steps, indicating the transgranular fracture behavior, which is similar to the fracture mode observed in many NiTi alloys[10,39]. These findings provide clear evidence that moderate B doping

refines the grains and promotes the enrichment of the secondary phases at grain boundaries. These secondary phases act as obstacles to dislocation motion and barriers to crack propagation, thereby enhancing grain boundary strength and improving the overall mechanical performance of the alloy.

The compressive stress-strain curve for the arc-melted $B_{1.5}$ alloy subjected to air cooling during annealing was also tested, as shown in Fig. 5(b). Under controlled composition and heat treatment, the suction-cast sample (green solid line) exhibited significantly higher fracture compressive strength and strain than the arc-melted sample (red dashed line). This indicates that the suction-casting process effectively refined the grains, thereby enhancing both the strength and toughness of the alloy. Furthermore, during the annealing process, different cooling methods (water cooling, air cooling, and furnace cooling) had a notable effect on the mechanical properties of the suction-cast $B_{1.5}$ alloy. Among these, the air-cooled samples achieved the highest fracture compressive strength and strain, followed by furnace-cooled, and water-cooled samples (Fig. 5(b)). Although the grain sizes of the water-cooled and air-cooled samples were similar (Fig. 3 (g) and (h)), their mechanical properties differed significantly. Due to the high cooling rate of water cooling, the sample undergoes significant thermal contraction during the cooling process. However, constrained by the size effect, there is a substantial difference in cooling rates between the core area and surface of the sample. This non-uniform cooling results in varying rates of volumetric shrinkage across different regions, and the resulting shrinkage gradient tends to induce residual thermal stresses and local defects within the sample, which adversely affect the mechanical properties of the alloy[40,41]. In contrast, the slow cooling rate of furnace cooling facilitates grain growth, weakening grain refinement strengthening and impairing the ability to deflect crack propagation, thereby lowering the strength and toughness. Air cooling, with a moderate cooling rate, effectively reduces thermal stress, prevents the formation of non-uniform microstructures, and maintains grain sizes comparable to water-cooled samples.

Moreover, the suction cast-air cooled sample is much stiffer than the other samples with the same composition. Microstructural analysis reveals that Mn_2B precipitates are present in all samples, as shown in Fig. S4. According to the literature, Mn_2B possesses a very high Young's modulus (about 498 GPa)[42], significantly exceeding that of the austenite in Ni-Mn-Sn alloy (generally below 200 GPa)[43,44]. The presence of this stiff secondary phase can substantially contribute to the overall elastic stiffness of the alloy. Among all samples, the suction cast-air cooled sample exhibits the highest area fraction of Mn_2B (approximately 4.1%), followed by the suction cast-water cooled (3.6%), arc

melted-air cooled (2.9%), and suction cast-furnace cooled (2.4%) samples. The increased fraction of this high-modulus secondary phase in the air-cooled sample enables it to carry more elastic load under applied stress, thus contributing to the observed higher macroscopic stiffness. However, despite having the second highest Mn_2B fraction, the suction cast-water cooled sample exhibits the lowest measured Young's modulus. This anomaly can be attributed to the residual thermal stress and local defects introduced during water quenching, which impair the effective elastic response of the austenitic matrix. For the other three samples (suction cast-air cooled, arc melted-air cooled, and suction cast-furnace cooled), the measured Young's modulus increases consistently with the Mn_2B area fraction. This clear correlation further supports that the area fraction of the secondary phase is the dominant factor influencing the elastic stiffness of these alloys. Overall, the fabrication process and the cooling rate during annealing can significantly affect the mechanical properties by regulating the microstructure of the alloy.

Thus, the combined effects of B alloying, suction casting, and air cooling during annealing effectively refine grains and introduce the secondary phases, providing an effective strategy to improve the alloy's strength and toughness. Accordingly, the subsequent analysis will focus on $(Ni_{43.5}Mn_{46}Sn_{10.5})_{100-x}B_x$ alloys prepared by suction casting and subjected to annealing with air cooling.

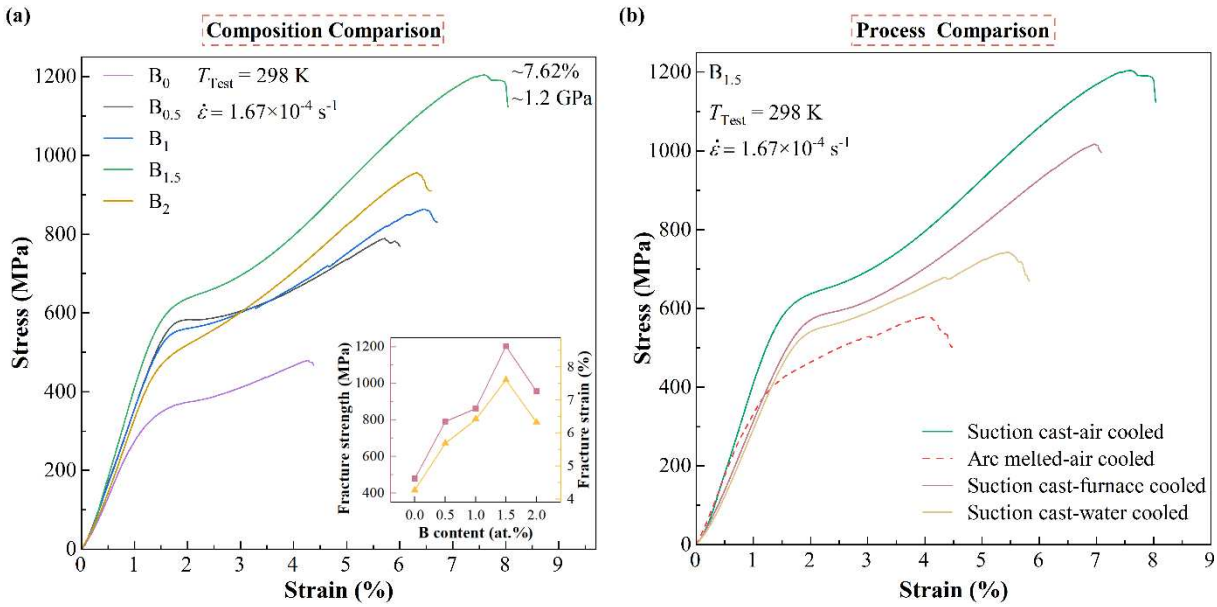

Fig. 5. Compression stress-strain curves under compression for (a) suction-cast $(Ni_{43.5}Mn_{46}Sn_{10.5})_{100-x}B_x$ (x=0, 0.5, 1, 1.5, 2) alloys subjected to air cooling during annealing and (b) $B_{1.5}$ alloy with different prepared methods and cooling rates during annealing at room temperature (~298 K) under a strain rate of $1.67\times10^{-4}s^{-1}$.

3.3 Phase transformation

To investigate the influence of B alloying on martensitic transformation, the DSC curves of $(Ni_{43.5}Mn_{46}Sn_{10.5})_{100-x}B_x$ (x=0, 0.5, 1, 1.5, 2) alloys were measured during cooling and heating (see Fig. 6(a)), and the characteristic temperatures (M_s, M_f, A_s, and A_f) and transformation entropy change ($\triangle S_{tr}$) for the martensitic transformation are summarized in Table 1. Results show that all alloys undergo martensitic transformation below room temperature, creating conditions suitable for exploring elastocaloric and superelastic response near room temperature. With increasing B content, both endothermic and exothermic peaks progressively shift to higher temperatures, leading to a corresponding increase in the martensitic transformation temperature (T_M=(M_s+M_f+A_s+A_f)/4) (Fig. 6(b)). In addition, the transformation interval ($\triangle T_{Int}$, defined by M_s-M_f) widens with increasing B content. For instance, the $\triangle T_{Int}$ for the $B_{1.5}$ and B_2 alloys reach 31.50 and 33.22 K, respectively, which are significantly higher than the 10.2 K of the B_0 alloy, mainly due to the inhibitory effect on the martensitic transformation by secondary phases. The widened martensitic transformation temperature window is expected to improve the controllability of shape memory alloys in actuation applications[45]. As shown in the inset in Fig. 6(a), the Curie temperature (T_C) of austenite also increases slightly with higher B content. This is attributed to B atoms occupying interstitial sites, which expands the lattice volume and causes the Mn-Mn distances to increase, thereby strengthening ferromagnetic coupling. Notably, the T_C of all alloys is greater than M_s, indicating the potential for magnetic-structural coupling transition. The $\triangle S_{tr}$ can be calculated from the endothermic peak using the formula $\triangle S_{tr}=\triangle H/T_0$, where $\triangle H$ represents the transformation enthalpy of the phase transition obtained by numerical integration of the endothermic peak, and T_0=(A_s+A_f)/2. The variation of $\triangle S_{tr}$ with B content is depicted by the magenta line in Fig. 6(b), where $\triangle S_{tr}$ decreases from 34.88 $Jkg^{-1}K^{-1}$ for B_0 alloy to 29.29 $Jkg^{-1}K^{-1}$ for B_2 alloy as B content increases. This reduction is primarily due to the increase of the secondary phase that does not undergo transformation, thereby reducing the volume fraction of the matrix that undergoes phase transformation.

Combining the analysis of Sections 3.2 and 3.3, the $B_{1.5}$ alloy demonstrates significant advantages in terms of microstructure, mechanical properties, and martensitic transformation behavior. The presence of fine grains and secondary phases enrichment at grain boundaries enhances its strength, resulting in the highest fracture compressive strength and strain among the studied alloys. Moreover, its near-room-temperature transformation, moderate $\triangle S_{tr}$, and broad $\triangle T_{Int}$ provide the $B_{1.5}$

alloy with excellent conditions for achieving significant elastocaloric effects, so its elastocaloric properties will be further analyzed in the following section.

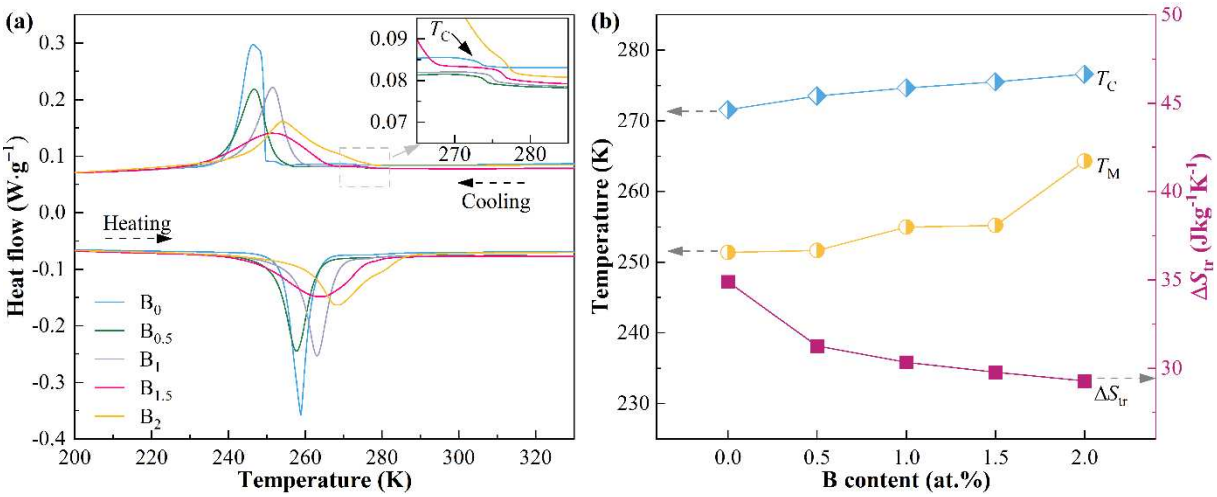

Fig. 6. (a) DSC curves for $(Ni_{43.5}Mn_{46}Sn_{10.5})_{100-x}B_x$ (x=0, 0.5, 1, 1.5, 2) alloys, with the inset highlighting the Curie transition temperature range. (b) Variation of Curie temperature (T_C), martensitic transformation temperature (T_M), and transformation entropy change ($\triangle S_{tr}$) with increasing B content.

Table 1 Martensitic transformation characteristic temperatures and transformation entropy change for $(Ni_{43.5}Mn_{46}Sn_{10.5})_{100-x}B_x$ (x=0, 0.5, 1, 1.5, 2) alloys.

Alloys	M_s (K)	M_f (K)	A_s (K)	A_f (K)	T_M (K)	T_C (K)	$\triangle S_{tr}$ (Jkg^{-1}K^{-1})
B_0	249.61	239.41	253.54	263.04	251.40	271.56	34.88
$B_{0.5}$	252.61	239.14	251.76	263.21	251.68	273.52	31.26
B_1	255.21	242.72	255.21	266.75	254.97	274.64	30.33
$B_{1.5}$	265.81	234.31	244.41	276.27	255.20	275.53	29.78
B_2	275.29	242.07	255.91	283.95	264.31	276.63	29.29

3.4 Superelasticity and elastocaloric effect

Fig. 7(a) shows the stress-strain curve of the $B_{1.5}$ alloy during 10 loading-unloading cycles with 3% compressive strain. A distinct plateau appears during loading in the first cycle, indicating the occurrence of stress-induced martensitic transformation (SIMT). However, approximately 0.7% residual strain remains upon unloading. With increasing training cycles, the residual strain gradually diminishes. At the 10th cycle, the stress-strain curve exhibits stable superelasticity with a recoverable strain of 2.1% without residual strain, which is favorable for achieving stable elastocaloric effect. Comparing the stress-strain curves from the 1st and 10th cycles, the critical driving stress (σ_{cr}) required for SIMT decreases from 600 MPa to 207 MPa, a reduction of 393 MPa (approximately 65.5%). Meanwhile, the energy dissipation $\triangle W$, defined as the enclosed area between loading and unloading stress-strain curve, decreases from 7.30 MJ/m³ to 1.28 MJ/m³, an 82% reduction. Analysis

of σ_{cr} and $\triangle W$ over the entire cycling process (as shown in Fig. 7(b)) reveals a significant drop after the first cycle, followed by stabilization in subsequent cycles. This is because the dislocations and residual martensite formed during the first cycle are positioned in "favorable" locations, generating beneficial internal stresses that facilitate subsequent phase transformations[46]. As a result, σ_{cr} experiences a sharp decline in the second cycle. From the second cycle onward, these dislocations and residual martensite gradually stabilize, ceasing to change after a certain number of cycles, which explains the observed stabilization in later cycles. Since $\triangle W$ is related to the frictional work during the movement of the phase interface and the plastic work at the austenite/martensite interface due to the loss of coherency, its reduction contributes to improved cyclic life and stability[15].

Fig. 7(c) presents the stress-strain response at room temperature under identical loading-unloading conditions with a strain rate of 1.0×10^{-3} s^{-1} for different strains. The compression strain was initially applied at 1.5% and then incrementally increased. When the strain reached 3%, the deformation of the alloy could be completely recovered after unloading, indicating superelastic behavior. However, when the strain was further increased to 3.5%, the shape recovery became incomplete after unloading, with a residual strain of approximately 0.1%. As shown in Fig. S5, the B_0 alloy also exhibited residual strain at a strain of 3%. These results indicate that the residual strain is attributed to the applied strain exceeding the recoverable transformation strain limit of the alloy. Beyond this limit, the stress-induced martensitic transformation cannot fully reverse upon unloading, leading to retained martensite. In addition, large applied strains promote dislocation generation and accumulation in the alloy, resulting in irreversible plastic deformation. In contrast to the typical plateau-type superelastic behavior of Ni-Mn-based alloys[14,47,48] and the stress-strain curve of B_0 alloy in Supplementary Fig. S6, the $B_{1.5}$ alloy exhibits a more linear stress-strain response. Such difference in superelasticity is primarily attributed to the changes in grain size and the increased phase transformation barrier due to the precipitation of the secondary phase. Section 3.2 analysis confirms that the $B_{1.5}$ alloy exhibits finer grain size compared to B_0, and the $B_{1.5}$ alloy has no preferred orientation. Therefore, when stress is applied to the non-textured fine-grained $B_{1.5}$ alloy, martensitic nucleation can occur continuously between grains, rather than exhibiting a plateau corresponding to an abrupt martensitic transformation in the stress-strain curve[49]. Moreover, grain refinement enhances the suppression of SIMT, requiring higher stress to induce phase transformation, which in turn increases the slope of the transformation plateau[50]. Additionally, the secondary phase continues

to bear external loads through elastic deformation as the austenite transforms into martensite, further contributing to the more linear stress-strain behavior of the $B_{1.5}$ alloy.

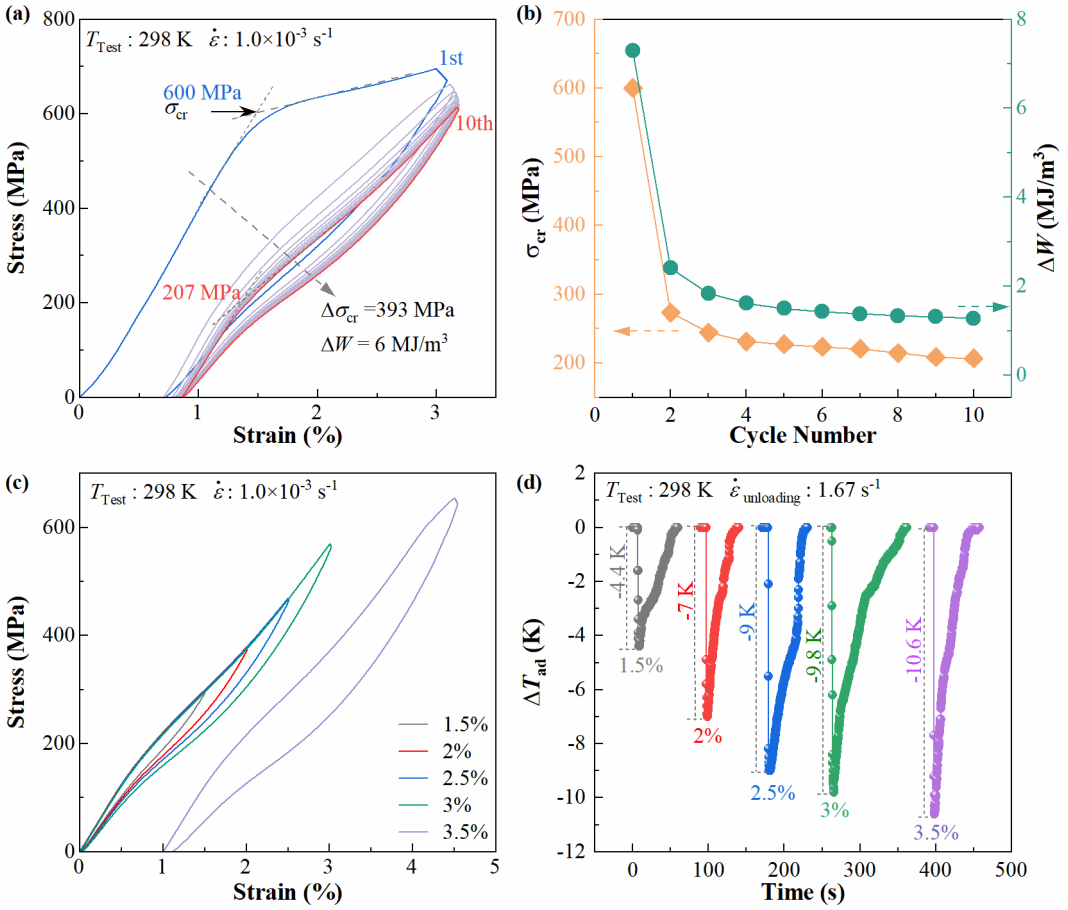

Fig. 7. (a) Compressive stress-strain curves measured during 10 loading-unloading cycles, (b) the variation in σ_{cr} and ΔW during mechanical training, (c) superelastic response at various compressive strains, (d) ΔT_{ad} profiles upon unloading measured under various compressive strains at 298 K for $(Ni_{43.5}Mn_{46}Sn_{10.5})_{98.5}B_{1.5}$ alloy.

Generally, large strain and high loading rate promote a significant elastocaloric effect[51]. However, an excessively high loading rate can induce fracture during the loading process. To balance these factors, a strategy combining slow loading (strain rate of 1.0 × 10^{-3} s^{-1}) and rapid unloading (strain rate of 1.67 s^{-1}) is employed to achieve quasi-adiabatic conditions, thereby maximizing adiabatic temperature changes. Fig. 7(d) shows the variation of $|\Delta T_{ad}|$ over time for the $B_{1.5}$ alloy under different strains with unloading. The results show that the ΔT_{ad} changes from -4.4 K at 1.5% strain to -9.8 K at 3% strain. This positive correlation between $|\Delta T_{ad}|$ and the applied strain is attributed to the increasing volume fraction of stress-induced martensite with higher strain, which leads to a greater latent heat absorption during the reverse martensitic transformation. Moreover, the reversible $|\Delta T_{ad}|$ of 9.8 K demonstrated in this work surpasses that previously reported for $(Ni_{43}Mn_{47}Sn_{10})_{99.5}Tb_{0.5}$ (5.5 K)[49], $Ni_{44}Mn_{41}Sn_{11}Cu_4$ (8 K)[52], and $Ni_{43}Co_6Mn_{40}Sn_{11}$ (7.1 K)[53], and

is comparable to single-crystalline $Ni_{57}Mn_{18}Ga_{21}In_4$ (9.6 K)[54] and $Ni_{50}Fe_{19}Ga_{27}Co_4$ (10.2 K)[55].

We now expand our investigation beyond room temperature to cover a broad temperature range from 278 K to 368 K. Fig. 8(a) presents the superelasticity stress-strain curves of the $B_{1.5}$ alloy at various test temperatures (T_{test}) with an interval of 10 K. Prior to all measurements, only one-time 10-cycles mechanical training was performed at room temperature. Throughout testing, the applied strain and strain rate are maintained at 3% and 1×10^{-3} s^{-1}, respectively. Notably, the $B_{1.5}$ alloy demonstrates excellent superelasticity over a wide temperature range of 80 K (288 K-368 K), as highlighted by the shaded light blue region. This characteristic is beneficial for achieving elastocaloric refrigeration over a wide temperature range. However, a partial unrecovered strain of approximately 0.1% was observed after unloading when T_{test}=278 K, likely originating from the enhanced thermodynamic stability of martensite at lower temperatures[56]. As shown in Figs. 8(b) and (c), within the temperature range where fully reversible martensitic transformations occurred (~80 K), the mean $\triangle T_{ad}$ of approximately -8.1 K, indicating excellent elastocaloric performance over a wide temperature range. The maximum ΔT was observed at 308 K (-10 K), which is close to the ΔT value measured at room temperature (298 K, -9.8 K), suggesting the alloy exhibits slightly superior elastocaloric effects at or slightly above room temperature.

Fig. 8(c) illustrates the temperature dependence of the critical driving stress (σ_{cr}) for superelasticity in the $B_{1.5}$ alloy. As the T_{test} increases from 288 K to 368 K, σ_{cr} rises linearly from 165 MPa to 412 MPa. This behavior is attributed to the enhanced stability of the austenitic at higher temperatures, which requires greater driving stresses to induce the martensitic transformation. The temperature sensitivity coefficient of σ_{cr}, defined as $d\sigma_{cr}/dT$, is determined to be 2.96 MPa/K. Such $d\sigma_{cr}/dT$ is lower than those in Ni-Mn-based FMSMAs (e.g., $Ni_{50}Mn_{35}In_{15}$ with $d\sigma_{cr}/dT$=5.19 MPa/K[57] and $Ni_{50}Mn_{31.5}In_{16}Cu_{2.5}$ with $d\sigma_{cr}/dT$=5.5 MPa/K[58]). The relatively low $d\sigma_{cr}/dT$ enables stable critical driving stress response over wide temperatures, improving the temperature adaptability and operating reliability of elastocaloric cooling devices.

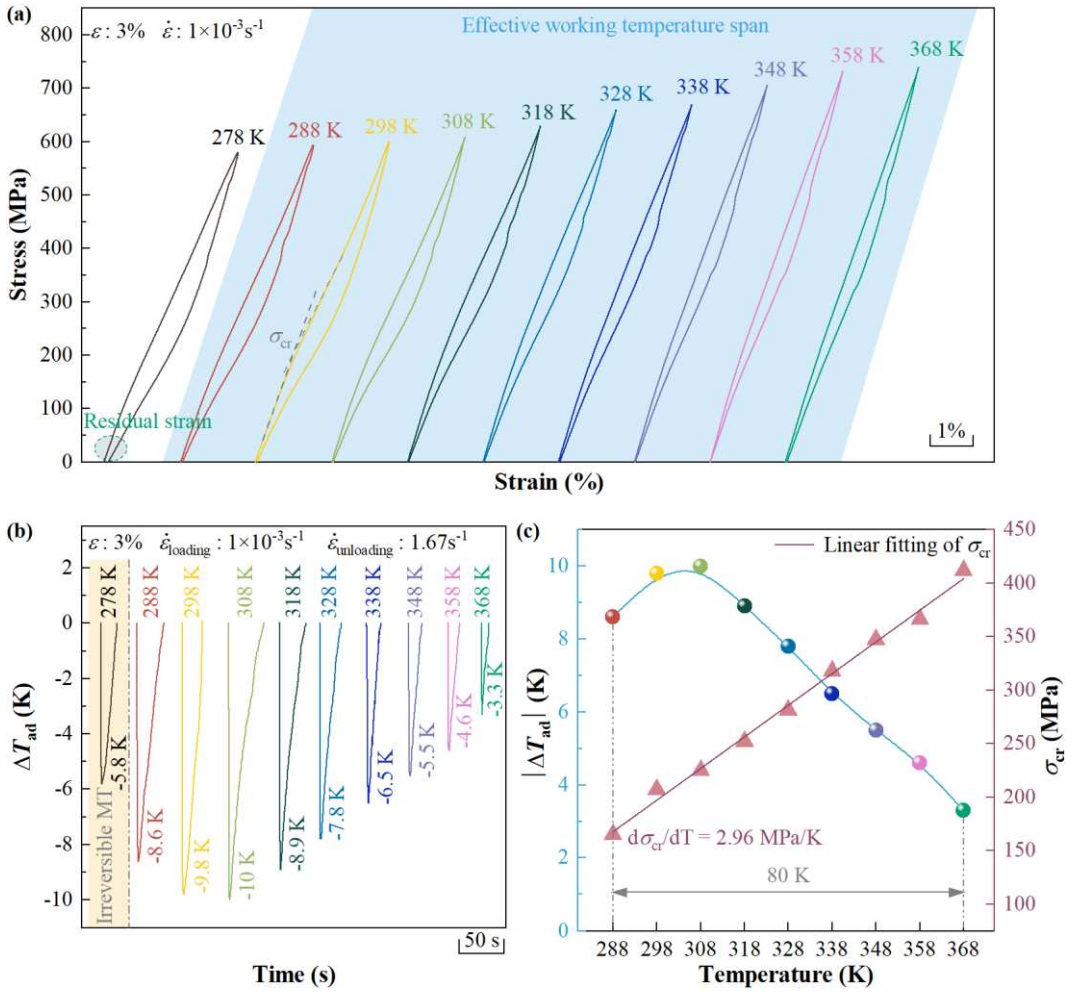

Fig. 8. (a) Temperature-dependent superelasticity stress-strain curves, (b) $\triangle T_{ad}$ profiles upon unloading measured under various compressive strains at various test temperatures, (c) Temperature dependences of σ_{cr} and $|\triangle T_{ad}|$ for $(Ni_{43.5}Mn_{46}Sn_{10.5})_{98.5}B_{1.5}$ alloy.

3.5 Cyclic stability of elastocaloric response

The long-term stability of superelastic performance is crucial for practical applications. To evaluate the cyclic behavior of eCE, fatigue tests were performed on the $B_{1.5}$ alloy over 10^5 consecutive loading-unloading cycles. This cycle number was chosen as an order-of-magnitude limit for the cycle tests, because achieving 10^6 cycles under the testing conditions is extremely difficult, and specimens of the same alloy were observed to develop surface microcracks between 100,000 and 110,000 cycles during repeated tests. Fig. 9(a) and (b) illustrate the change in the superelastic curve and $|\triangle T_{ad}|$ profiles upon unloading before and after 10^5 cycles. The results indicate that the alloy maintains stable superelasticity, with only a slight decrease in maximum strain (0.09%) and a small reduction in $|\triangle T_{ad}|$ (0.6 K), demonstrating excellent functional stability after 10^5 cycles. Fig. 9(c) compares the corresponding cyclic $|\triangle T_{ad}|$ and cyclic stability of the alloy with other typical elastocaloric materials from the literature. The comparison reveals that the alloy maintains a high

$|\Delta T_{ad}|$ and significantly outperforms other Ni-Mn-based and Ni-Fe-based FMSMAs in terms of cyclic stability. While polycrystalline FMSMAs generally endure 10^2-10^3 cycles, and single-crystal FMSMAs can withstand up to 10^4 cycles. In contrast, the polycrystalline alloy in this study demonstrates remarkable cyclic stability up to 10^5 cycles, an order of magnitude higher than single-crystal alloys.

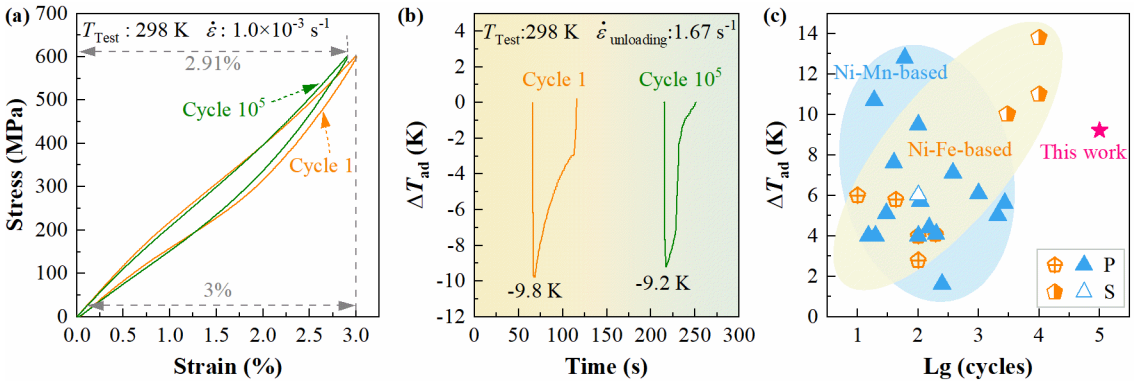

Fig. 9. Compressive stress-strain curves (a) and elastocaloric cooling of $(Ni_{43.5}Mn_{46}Sn_{10.5})_{98.5}B_{1.5}$ alloy before and after 10^5 cycles. (c) Comparison of elastocaloric cycling stability between $B_{1.5}$ alloy and other ferromagnetic shape memory alloys, including Ni-Mn-based (P)[11-14,53,59-67], Ni-Mn-based (S)[68], Ni-Fe-based (P)[69-71], and Ni-Fe-based (S)[55,72,73] FMSMAs, where P and S stand for polycrystal and single crystal.

The superior cyclability of the $B_{1.5}$ alloy is directly attributed to its enhanced mechanical properties, which preserve functional integrity and prevent fracture during repeated cycling loading. Additionally, the low dissipated energy fraction ($\Delta W/W$) is a key factor contributing to the long-term stability of the alloy. $\Delta W/W$ is defined as the ratio of dissipated energy (ΔW, corresponding to the enclosed region between the loading and unloading stress-strain curves) to the total applied energy (W, corresponding to the area under the loading curve during a mechanical cycle). In the present alloy, $\Delta W/W$ is as low as 17.7%, significantly lower than that of $Ni_{50}Mn_{34.8}In_{15.2}$ (41.9% of 40 cycles)[11] and $Ni_{54}Fe_{19}Ga_{27}$ (20.4% of 20,000 cycles)[74]. The relatively low $\Delta W/W$ extends fatigue life by minimizing internal interface friction and improving resistance to lattice defect formation[75]. Notably, a $Ni_{51.5}Ti_{48.5}/Ni_3Ti$ nanocomposite with an even lower $\Delta W/W$ of 6.9% enables stable linear superelasticity over 10^6 cycles[15]. Therefore, achieving a more linear superelastic response is an effective strategy for achieving excellent cycle stability.

To further investigate the factors contributing to the excellent cyclic stability, SEM analysis was performed on the sample that was cycled over 10^5 cycles. As shown in Fig. 10(a), micron-sized cracks were observed propagating along the grain boundaries. For comparison, the B_0 alloy was also examined, which exhibited macroscopically visible cracks on the surface after mechanical training. As shown in Fig. 10(b), the SEM images revealed significant crack propagation along the loading direction. This comparison provides clear evidence for the enhanced cyclic stability of the $B_{1.5}$ alloy resulting from grain refinement and introducing non-transforming secondary phases. Smaller grain

sizes increase the number of grain boundaries that a crack must overcome more grain boundaries during propagation, increasing energy dissipation. The increased number of grain boundaries facilitates changes in the crack propagation path, reducing linear crack growth and making crack propagation more difficult. Further investigation revealed distinct crack propagation behaviors in the presence of the Mn_2B phase, as shown in Fig. 10(c) and (d). Before encountering the Mn_2B phase, cracks propagated in a straight line through the austenite matrix. However, upon reaching the Mn_2B phase, crack propagation stalled and deflected along the austenite/Mn_2B interface (purple circle). This suggests that the plastic deformation of Mn_2B may dissipate the energy required for crack propagation, effectively leading to crack blunting[76]. The interaction between the secondary phase and the crack is known as crack trapping[77]. In another case, the crack tip continued to propagate, leaving an intact Mn_2B phase in the crack wake (blue circle), which is called crack bridging[77,78]. The cohesive force of the Mn_2B phase impedes further crack extension during the bridging process. Additionally, cracks often deviate around the Mn_2B phase (red circle) and consume more energy. This energy dissipation mechanism slows down crack propagation, improving the material's toughness and fatigue performance. So, the various crack-suppressing effects of the Mn_2B phase significantly contribute to the superior cyclic stability of the $B_{1.5}$ alloy.

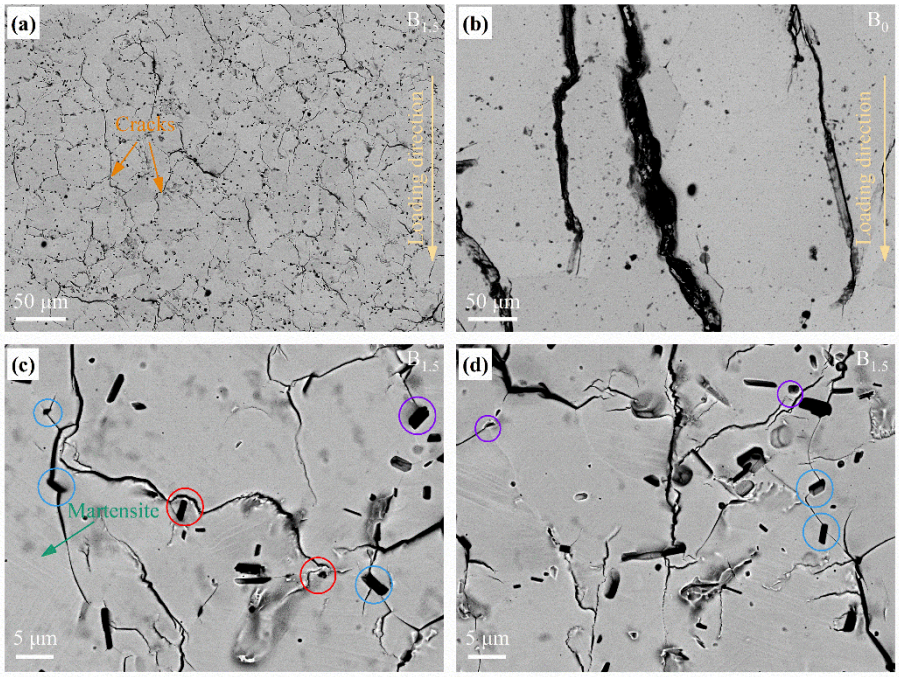

Fig. 10. BSE micrographs of (a) $B_{1.5}$ alloy after 10^5 cycles, (b) B_0 alloy after 10 cycles, and (c, d) enlarged crack propagation paths of $B_{1.5}$ alloy.

In summary, the simple suction casting technique, combined with B alloying and a controlled cooling rate during annealing, effectively achieved multiple grain refinement and the introduction of non-transforming Mn_2B secondary phases to reinforce grain boundaries, suppress crack propagation,

and achieved a more linear superelasticity. It should be pointed out that the multi-step process employed here for microstructure control is more time-efficient and cost-effective compared with those complex preparation processes involving nanoscale structures and textures. Furthermore, grain refinement via suction casting and alloying helps prevent severe deformation during the preparation process, reducing the mechanical performance requirements for the target material. Therefore, the combination of rapid solidification and B alloying offers a versatile approach suitable for various shape-memory alloys. In this context, this work not only presents an effective strategy for designing low-cost and high-performance polycrystalline brittle Heusler alloys, but also paves the way for the development of materials with excellent elastocaloric cyclic stability.

3.6 Phase transformation cycle stability

Since the superelasticity of the $B_{1.5}$ alloy originates from the martensitic transformation involving a structural transition, the cyclic stability of this transformation is critical for maintaining a reversible superelastic response. To assess this stability, the $B_{1.5}$ alloy was subjected to 50 cycles of DSC measurements, and the corresponding curves are shown in Fig. 11. It can be clearly observed that the endothermic and exothermic peaks are highly consistent during each cycle, indicating excellent cyclic stability of the martensitic transformation in the alloy. For comparison, the DSC curves of the B0 alloy after 50 cycles (Supplementary Fig. S7) exhibit noticeable misalignment of the exothermic peaks. This result further confirms the positive effect of grain refinement on the cyclic stability of functional behavior and explains the superior stability of the superelastic response in the $B_{1.5}$ alloy.

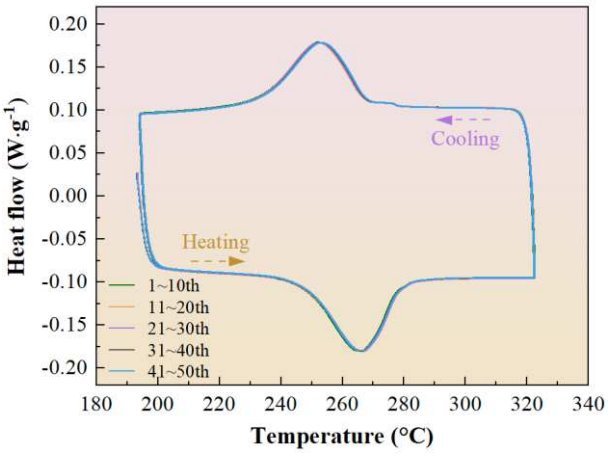

Fig. 11. DSC curves of 50 thermal cycles for $(Ni_{43.5}Mn_{46}Sn_{10.5})_{98.5}B_{1.5}$ alloy.

Martensitic transformation, as a first-order phase transition, is typically accompanied by transformation hysteresis, which is widely recognized as a key factor affecting the cycling stability of NiMn-based alloys. According to the geometrically nonlinear theory of martensitic transformation, both the transformation hysteresis and phase transformation reversibility are closely related to the

geometric compatibility between the austenite and martensite[79,80]. The geometric compatibility can be quantitatively evaluated using the middle eigenvalue (λ_2) of the transformation stretch matrix U. A λ_2 value closer to 1 indicates better geometric compatibility at the austenite-martensite interface[81]. Since the transformation stretch matrix U is constructed based on the lattice constants of the two phases, the geometric compatibility of the $B_{1.5}$ alloy was analyzed by powder XRD measurements at 298 K and 100 K, as shown in Fig. 12. The results reveal that the alloy undergoes a phase transformation from cubic austenite with $L2_1$ order to six-layer modulated (6M) martensite during cooling. From the XRD data, the lattice constant of austenite was determined to be a_A=6.003 Å, while the lattice constants of 6M martensite were a_M=4.418 Å, b_M=5.590 Å, c_M=12.976 Å, and β=92.869°. The cubic-to-monoclinic structural transformation can proceed through multiple variant configurations[82], among which the "Cube-edge" variant matrix is employed in this investigation, with transformation stretch matrix U can be constructed as follows[83]:

$$\mathrm{U}=\begin{pmatrix}\tau & \sigma & 0\\ \sigma & \rho & 0\\ 0 & 0 & \delta\end{pmatrix}$$

In the matrix, $\tau=\dfrac{\alpha^2+\gamma^2+2\alpha\gamma(\sin\beta-\cos\beta)}{2\sqrt{\alpha^2+\gamma^2+2\alpha\gamma\sin\beta}}$, $\rho=\dfrac{\alpha^2+\gamma^2+2\alpha\gamma(\sin\beta+\cos\beta)}{2\sqrt{\alpha^2+\gamma^2+2\alpha\gamma\sin\beta}}$, $\sigma=\dfrac{\alpha^2-\gamma^2}{2\sqrt{\alpha^2+\gamma^2+2\alpha\gamma\sin\beta}}$, and $\delta=\dfrac{b_M}{a_A}$, $\alpha=\dfrac{a_M\sqrt{2}}{a_A}$, $\gamma=\dfrac{c_M\sqrt{2}}{Na_A}$, due to the characteristics of the 6M martensite crystal structure, N is taken as 3 in the calculation. Based on these parameters, the transformation stretch matrix U was constructed as follows:

$$\mathrm{U}=\begin{pmatrix}1.0554 & 0.0109 & 0\\ 0.0109 & 1.0038 & 0\\ 0 & 0 & 0.9312\end{pmatrix}$$

The calculated λ_2 of the U is 1.0016, deviating from 1 by only 0.0016. This deviation is comparable to the 0.0023 difference observed in the $Ni_{40}Co_{10}Mn_{40}Sn_9Al_1$ alloy (λ_2=0.9977), which exhibits a thermal hysteresis of 12 K[84]. From the data in Table 1, the thermal hysteresis ($\Delta T_{hys}=(A_s+A_f-M_s-M_f)/2$) of the $B_{1.5}$ alloy is determined to be 10.28 K. These results confirm excellent geometric compatibility between the austenite and martensite, which ensures the $B_{1.5}$ alloy exhibits low thermal hysteresis. This explains the reversible and stable transformation during the numerous cycles without deleterious effects, thus achieving superior cyclic stability of large elastocaloric effect.

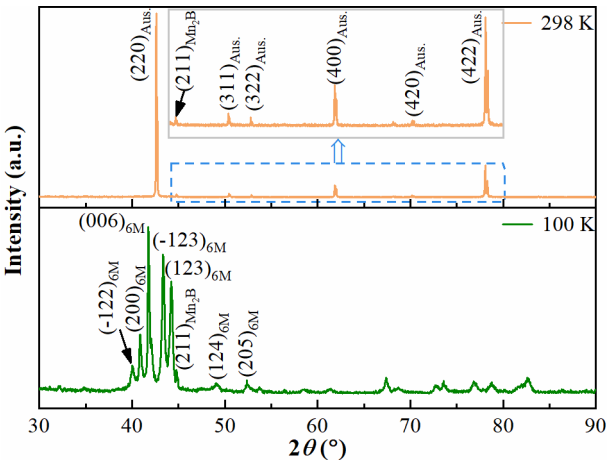

Fig. 12. Powder XRD patterns measured at 298 K and 100 K for $(Ni_{43.5}Mn_{46}Sn_{10.5})_{98.5}B_{1.5}$ alloy.

4. Conclusions

In this study, first-principles calculations revealed that the B atoms preferentially occupy the tetrahedral interstice formed by 2 Ni, 1 Mn_{Mn}, and 1 Mn_{Sn} atoms. Electronic structure analysis reveals that B doping induces localized lattice distortions and facilitates the formation of *d-d* bonds similar to metallic bonds. This significantly increases the B/G_v, P_c, and ν values, elucidating the underlying physical mechanism responsible for the enhanced mechanical properties due to B alloying. Fine-grained $(Ni_{43.5}Mn_{46}Sn_{10.5})_{100-x}B_x$ (x=0, 0.5, 1, 1.5, 2) alloys were prepared by suction casting, followed by air cooling during annealing. With increasing B content, grain size decreased and the amounts of Mn_2B precipitates increased. Consequently, the $B_{1.5}$ alloy exhibits superior mechanical properties, achieving a compressive strength of 1.2 GPa and a strain of 7.62%. At room temperature, the $B_{1.5}$ alloy exhibits a more linear stress-strain response compared to the typical plateau-type superelastic behavior observed in Ni-Mn-based alloys. A large ΔT_{ad} of -9.8 K was measured with excellent superelasticity of 3%. Moreover, the $B_{1.5}$ alloy displays fully reversible superelasticity and a large elastocaloric effect over a wide temperature range (288 K to 368 K), with a temperature window as large as 80 K. Within this range, the mean ΔT_{ad} approximately -8.1 K, reaching a maximum value of -10 K at 308 K. Cyclic testing revealed that the $B_{1.5}$ alloy maintained long-term stability over 10^5 superelastic cycles under 600 MPa compressive stress, with $|\Delta T_{ad}|$ decreasing only slightly from 9.8 K to 9.2 K, demonstrating superior cyclic stability compared to other Ni-Mn-based and Ni-Fe-based FMSMAs. These findings highlight that microstructure control through grain refinement effectively suppresses crack propagation. Moreover, the introduction of the non-transforming Mn_2B phase inhibits crack growth through mechanisms such as crack blunting, trapping, and bridging, thereby improving functional cyclic stability. The combined approach of suction casting and B alloying provides an effective microstructure engineering strategy for developing cost-efficient bulk materials

with high superelastic cyclic stability, making it applicable to a wide range of shape memory alloys.

Acknowledgments This work is financially supported by the National Natural Science Foundation of China (Grant No. 51771044), the Performance subsidy fund for Key Laboratory of Dielectric and Electrolyte Functional Material Hebei (No. 22567627H), Hebei Central Government-Guided Local Science & Technology Development Fund Project (246Z1026G), The Ministry of Education's "Chunhui Program" Collaborative Research Project (HZKY20220244).

Conflict of Interest The authors state that there are no conflicts of interest to disclose.

References

[1] P. Kabirifar, J. Trojer, M. Brojan, J. Tušek, From the elastocaloric effect towards an efficient thermodynamic cycle, J. Phys. Energy 4 (2022) 044009.

[2] F. Greibich, R. Schwödiauer, G. Mao, D. Wirthl, M. Drack, R. Baumgartner, A. Kogler, J. Stadlbauer, S. Bauer, N. Arnold, M. Kaltenbrunner, Elastocaloric heat pump with specific cooling power of 20.9 W g^{-1} exploiting snap-through instability and strain-induced crystallization, Nat. Energy 6 (2021) 260-267.

[3] G.Y. Zhang, D. Li, C. Liu, Z.B. Li, B. Yang, H.L. Yan, X. Zhao, L. Zuo, Giant low-field actuated caloric effects in a textured $Ni_{43}Mn_{47}Sn_{10}$ alloy, Scr. Mater. 201 (2021) 113947.

[4] Y.D. Zhu, H.C. Xuan, J.C. Su, F.H. Chen, K.W. Zhang, P.D. Han, J.W. Q, Large elastocaloric effect in as-cast Ni-Mn-Sn-Fe ferromagnetic shape memory alloys, Phys. Lett. A 451 (2022) 128374.

[5] W.Y. Gui, Y.H. Qu, Y.X. Cao, Y.Z. Zhao, C.X. Liu, Q. Zhou, J. Chen, Y.H. Liu, The effect of Tb substitution for Ni on microstructure, martensitic transformation and cyclic stability of elastocaloric effect in Ni-Mn-Sn magnetic shape memory alloys, J. Mater. Res. Technol. 19 (2022) 4998-5007.

[6] T. Waitz, V. Kazykhanov, H.P. Karnthaler, Martensitic phase transformations in nanocrystalline NiTi studied by TEM, Acta Mater. 52 (2004) 137-147.

[7] J.Y. Chen, L.P. Lei, G. Fang, Grain-size effects on the temperature-dependent elastocaloric cooling performance of polycrystalline NiTi alloy, J. Alloys Compd. 927 (2022) 166951.

[8] J.Y. Chen, L.P. Lei, G. Fang, D.W. Wang, Achieving great comprehensive elastocaloric cooling performances of superelastic NiTi by grain size engineering, Mater. Today Nano 21 (2023)

100279.

[9] H.Y. Lin, P. Hua, Q.P. Sun, Effects of grain size and partial amorphization on elastocaloric cooling performance of nanostructured NiTi, Scr. Mater. 209 (2022) 114371.

[10] K. Zhang, G.Z. Kang, Q.P. Sun, High fatigue life and cooling efficiency of NiTi shape memory alloy under cyclic compression, Scr. Mater. 159 (2019) 62-67.

[11] X.M. Huang, L.D. Wang, H.X. Liu, H.L. Yan, N. Jia, B. Yang, Z.B. Li, Y.D. Zhang, C. Esling, X. Zhao, L. Zuo, Correlation between microstructure and martensitic transformation, mechanical properties and elastocaloric effect in Ni-Mn-based alloys, Intermetallics 113 (2019) 106579.

[12] Z. Yang, D.Y. Cong, X.M. Sun, Z.H. Nie, Y.D. Wang, Enhanced cyclability of elastocaloric effect in boron-microalloyed Ni-Mn-In magnetic shape memory alloys, Acta Mater. 127 (2017) 33-42.

[13] Z. Yang, D.Y. Cong, Y. Yuan, Y. Wu, Z.H. Nie, R.G. Li, Y.D. Wang, Ultrahigh cyclability of a large elastocaloric effect in multiferroic phase-transforming materials, Mater. Res. Lett. 7 (2019) 137-144.

[14] X.M. Huang, Y. Zhao, H.L. Yan, N. Jia, S. Tang, J. Bai, B. Yang, Z.B. Li, Y.D. Zhang, C. Esling, X. Zhao, L. Zuo, A multielement alloying strategy to improve elastocaloric and mechanical properties in Ni-Mn-based alloys via copper and boron, Scr. Mater. 185 (2020) 94-99.

[15] H.L. Hou, E. Simsek, T. Ma, N.S. Johnson, S.X. Qian, C. Cissé, D. Stasak, N. Al Hasan, L. Zhou, Y.H. Hwang, R. Radermacher, V.I. Levitas, M.J. Kramer, M.A. Zaeem, A.P. Stebner, R.T. Ott, J. Cui, I. Takeuchi, Fatigue-resistant high-performance elastocaloric materials made by additive manufacturing, Science 366 (2019) 1116-1121.

[16] G. Kresse, D. Joubert, From ultrasoft pseudopotentials to the projector augmented-wave method, Phys. Rev. B 59 (1999) 1758-1775.

[17] J. Hafner, Atomic-scale computational materials science, Acta Mater. 48 (2000) 71-92.

[18] P.E. Blöchl, Projector augmented-wave method, Phys. Rev. B 50 (1994) 17953.

[19] G. Kern, G. Kresse, J. Hafner, Ab initio calculation of the lattice dynamics and phase diagram of boron nitride, Phys. Rev. B 59 (1999) 8551-8559.

[20] J.P. Perdew, K. Burke, M. Ernzerhof, Generalized gradient approximation made simple, Phys. Rev. Lett. 77 (1996) 3865-3868.

[21] S. Özdemir Kart, M. Uludoğan, I. Karaman, T. Çağın, DFT studies on structure, mechanics and phase behavior of magnetic shape memory alloys: Ni_2MnGa, Phys. Stat. Sol. (a) 205 (2008) 1026-1035.

[22] Y. Zhang, J. Bai, Z.Q. Guan, X.Z. Liang, Y.S. Li, J.L. Gu, Y.D. Zhang, C. Esling, X. Zhao, L. Zuo, Phase stability, magnetic properties, and martensitic transformation of $Ni_{2-x}Mn_{1+x+y}Sn_{1-y}$ Heusler alloy with excess Mn by first-principles calculations, Acta. Metall. Sin-Engl. 36 (2023) 513-528.

[23] H.L. Yan, X.M. Huang, C. Esling, Recent progress in crystallographic characterization, magnetoresponsive and elastocaloric effects of Ni-Mn-In-based Heusler alloys—A review, Front. Mater. 9 (2022) 812984.

[24] S. Ghosh, S. Ghosh, Understanding the origin of the magnetocaloric effects in substitutional Ni-Mn-Sb-Z (Z=Fe, Co, Cu) compounds: Insights from first-principles calculations, Phys. Rev. B 101 (2020) 024109.

[25] D.Y. Cong, W.X. Xiong, A. Planes, Y. Ren, L. Manosa, P.Y. Cao, Z.H. Nie, X.M. Sun, Z. Yang, X.F. Hong, Y.D. Wang, Colossal elastocaloric effect in ferroelastic Ni-Mn-Ti alloys, Phys. Rev. Lett. 122 (2019) 255703.

[26] T. Roy, M.E. Gruner, P. Entel, A. Chakrabarti, Effect of substitution on elastic stability, electronic structure and magnetic property of Ni-Mn based Heusler alloys: An ab initio comparison, J. Alloys Compd. 632 (2015) 822-829.

[27] T. Roy, D. Pandey, A. Chakrabarti, Probing the possibility of coexistence of martensite transition and half-metallicity in Ni and Co-based full-Heusler alloys: An ab initio calculation, Phys. Rev. B 93 (2016) 184102.

[28] Q. Mahmood, M. Yaseen, Bakhtiar Ul Haq, A. Laref, Aalia Nazir, The study of mechanical and thermoelectric behavior of $MgXO_3$ (X = Si, Ge, Sn) for energy applications by DFT, Chem. Phys. 524 (2019) 106-112.

[29] D.G. Pettifor, Bonding and structure of molecules and solids, Oxford University Press, 1995.

[30] R.H. Baughman, J.M. Shacklette, A.A. Zakhidov, S. Stafström, Negative Poisson's ratios as a common feature of cubic metals, Nature 392 (1998) 362-365.

[31] G.J. Li, L. Xu, Z.H. Cao, A unified physical mechanism for martensitic phase transition and ductility in Ni-Mn-based ferromagnetic shape memory alloys: the case of Cu-doped Ni_2MnGa, J. Mater. Chem. C. 11 (2023) 6173-6182.

[32] H.L. Yan, H.X. Liu, Y. Zhao, N. Jia, J. Bai, B. Yang, Z.B. Li, Y.D. Zhang, C. Esling, X. Zhao, L. Zuo, Impact of B alloying on ductility and phase transition in the Ni-Mn-based magnetic shape memory alloys: Insights from first-principles calculation, J. Mater. Sci. Technol. 74 (2021) 27-34.

[33] P. Bate, The effect of deformation on grain growth in Zener pinned systems, Acta Mater. 49 (2001) 1453-1461.

[34] S. Öztürk, K. İcin, M. Gençtürk, M. Göbülük, U. Topal, P. Svec, Surface and structural characterization of amorphous Fe, Co-based melt-spun ribbons subjected to heat treatment processes, J. Non-Cryst. Solids 522 (2019) 119592.

[35] W.H. Yang, G.H. Zhao, Y.P. Wang, S.K. Wang, S.S. Zhan, D. Wang, M.D. Bao, B. Tang, L.J. Yao, X.Z. Wang, Influence of grain size of Cu target on its magnetron sputtering erosion and

parameters, J. Mater. Sci-Mater. El. 32 (2021) 26181-26188.

[36] J.Y. Chen, H. Yin, Q.P. Sun, Effects of grain size on fatigue crack growth behaviors of nanocrystalline superelastic NiTi shape memory alloys, Acta Mater. 195 (2020) 141-150.

[37] H.C. Xuan, D.H. Wang, C.L. Zhang, Z.D. Han, B.X. Gu, Y.W. Du, Boron's effect on martensitic transformation and magnetocaloric effect in $Ni_{43}Mn_{46}Sn_{11}B_x$ alloys, Appl. Phys. Lett. 92 (2008) 102503.

[38] G. Kirat, O. Kizilaslan, M.A. Aksan, Magnetoresistance properties of magnetic Ni-Mn-Sn-B shape memory ribbons and magnetic field sensor aspects operating at room temperature, J. Magn. Magn. Mater. 477 (2019) 366-371.

[39] B. Haghgouyan, B. Young, S. Picak, T. Baxevanis, I. Karaman, D.C. Lagoudas, A unified description of mechanical and actuation fatigue crack growth in shape memory alloys, Acta Mater. 217 (2021) 117155.

[40] A. Samuel, K.N. Prabhu, Residual stress and distortion during quench hardening of steels: A review, J. Mater. Eng. Perform. 31 (2022) 5161-5188.

[41] S. Zinn, Quenching of induction heated steel, in: V. Rudnev, G.E. Totten(Eds), Induction Heating and Heat Treatment, ASM International, Ohio, 2014, pp.87-128.

[42] B. Wang, X. Li, Y.X. Wang, Y.F. Tu, Phase stability and physical properties of manganese borides: A first-principles study, J. Phys. Chem. C. 115 (2011) 21429-21435.

[43] C.M. Li, Q.M. Hu, R. Yang, B. Johansson, L. Vitos, Theoretical investigation of the magnetic and structural transitions of Ni-Co-Mn-Sn metamagnetic shape-memory alloys, Phys. Rev. B 92 (2015) 024105.

[44] Y. Zhang, J. Bai, K.L. Guo, D. Liu, J.L. Gu, N. Morley, Q.S. Ma, Q.Z. Gao, Y.D. Zhang, C. Esling, X. Zhao, L. Zuo, An alloying strategy for tuning magnetism, thermal hysteresis, and mechanical properties in Ni-Mn-Sn-based Heusler alloys, J. Alloys Compd. 979 (2024) 173593.

[45] B.S. Shariat, Q.L. Meng, A.S. Mahmud, Z.G. Wu, R. Bakhtiari, J.S. Zhang, F. Motazedian, H. Yang, G. Rio, T. Nam, Y.N. Liu, Functionally graded shape memory alloys: Design, fabrication and experimental evaluation, Mater. Design. 124 (2017) 225-237.

[46] J. Ma, I. Karaman, R.D. Noebe, High temperature shape memory alloys, Int. Mater. Rev. 55 (2010) 257-315.

[47] D.W. Zhao, J. Liu, Y. Feng, W. Sun, A. Yan, Giant elastocaloric effect and its irreversibility in [001]-oriented $Ni_{45}Mn_{36.5}In_{13.5}Co_5$ meta-magnetic shape memory alloys, Appl. Phys. Lett. 110 (2017) 021906.

[48] G.Y. Zhang, Z.B. Li, J.J. Yang, B. Yang, D.H. Wang, Y.D. Zhang, C. Esling, L. Hou, X. Li, X. Zhao, L. Zuo, Giant elastocaloric effect in a Mn-rich $Ni_{44}Mn_{46}Sn_{10}$ directionally solidified alloy, Appl. Phys. Lett. 116 (2020) 023902.

[49] H.Y. Qian, R. Cai, X. Lu, W. Sun, G.W. Li, Z.Y. Wei, Unveiling the enhancing mechanism of cyclic stability in Tb doped Ni-Mn-Sn Heusler alloys, Mater. Design. 244 (2024) 113162.

[50] A. Aslan, Q.P. Sun, Stress hysteresis and temperature dependence of phase transition stress in nanostructured NiTi—Effects of grain size, Appl. Phys. Lett. 103 (2013) 021902.

[51] J.J. Yang, H.L. Wang, Z.B. Li, N.F. Zou, H.L. Yan, B. Yang, L. Zuo, Crystallography of stress-induced martensitic transformation and giant elastocaloric effect in a $<001>_A$ textured $Ni_{27}Cu_{21}Mn_{46}Sn_6$ shape memory alloy, Acta Mater. 263 (2024) 119546.

[52] Y. Li, W. Sun, D.W. Zhao, H. Xu, J. Liu, An 8 K elastocaloric temperature change induced by 1.3% transformation strain in $Ni_{44}Mn_{45-x}Sn_{11}Cu_x$ alloys, Scr. Mater. 130 (2017) 278-282.

[53] Y.H. Qu, D.Y. Cong, S.H. Li, W.Y. Gui, Z.H. Nie, M.H. Zhang, Y. Ren, Y.D. Wang, Simultaneously achieved large reversible elastocaloric and magnetocaloric effects and their coupling in a magnetic shape memory alloy, Acta Mater. 151 (2018) 41-55.

[54] J.M. Wang, Q. Yu, K.Y. Xu, C.Zhang, Y.Y. Wu, C.B. Jiang, Large room-temperature elastocaloric effect of $Ni_{57}Mn_{18}Ga_{21}In_4$ alloy undergoing a magnetostructural coupling transition, Scr. Mater. 130 (2017) 148-151.

[55] F. Xiao, M.J. Jin, J. Liu, X.J. Jin, Elastocaloric effect in $Ni_{50}Fe_{19}Ga_{27}Co_4$ single crystals, Acta Mater. 96 (2015) 292-300.

[56] H.Y. Xiang, Y.X. Guo, X.L. Zhao, Z.B. Li, B. Yang, N. Jia, H.L. Yan, L. Zuo, Large low-stress elastocaloric effect in Ti-Zr-Cr-Sn, Scr. Mater. 244 (2024) 116002.

[57] Z.Z. Li, Z.B. Li, D. Li, J.J. Yang, B. Yang, Y. Hu, D.H. Wang, Y.D. Zhang, C. Esling, X. Zhao, L. Zuo, Achieving a broad refrigeration temperature region through the combination of successive caloric effects in a multiferroic $Ni_{50}Mn_{35}In_{15}$ alloy, Acta Mater. 192 (2020) 52-59.

[58] D.W. Zhao, J. Liu, X. Chen, W. Sun, Y. Li, M.X. Zhang, Y.Y. Shao, H. Zhang, A. Yan, Giant caloric effect of low-hysteresis metamagnetic shape memory alloys with exceptional cyclic functionality, Acta Mater. 133 (2017) 217-223.

[59] D. Li, Z.B. Li, J.J. Yang, Z.Z. Li, B. Yang, H.L. Yan, D.H. Wang, L. Hou, X. Li, Y.D. Zhang, C. Esling, X. Zhao, L. Zuo, Large elastocaloric effect driven by stress-induced two-step structural transformation in a directionally solidified $Ni_{55}Mn_{18}Ga_{27}$ alloy, Scr. Mater. 163 (2019) 116-120.

[60] L.S. Wei, X.X. Zhang, W.M. Gan, C. Ding, L. Geng, Hot extrusion approach to enhance the cyclic stability of elastocaloric effect in polycrystalline Ni-Mn-Ga alloys, Scr. Mater. 168 (2019) 28-32.

[61] Y. Hu, Z.B. Li, B. Yang, S.X. Qian, W.M. Gan, Y.Y. Gong, Y. Li, D.W. Zhao, J. Liu, X. Zhao, L. Zuo, D.H. Wang, Y.W. Du, Combined caloric effects in a multiferroic Ni-Mn-Ga alloy with broad refrigeration temperature region, APL Mater. 5 (2017) 046103.

[62] L.S. Wei, X.X. Zhang, J. Liu, L. Geng, Orientation dependent cyclic stability of the elastocaloric

effect in textured Ni-Mn-Ga alloys, AIP Adv. 8 (2018) 055312.

[63] B.F. Lu, P.N. Zhang, Y. Xu, W. Sun, J. Liu, Elastocaloric effect in $Ni_{45}Mn_{36.4}In_{13.6}Co_5$ metamagnetic shape memory alloys under mechanical cycling, Mater. Lett. 148 (2015) 110-113.

[64] X.H. Tang, Y. Feng, H.B. Wang, P. Wang, Enhanced elastocaloric effect and cycle stability in B and Cu co-doping Ni-Mn-In polycrystals, Appl. Phys. Lett. 114 (2019) 033901.

[65] Y.H. Qu, A. Gràcia-Condal, L. Mañosa, A. Planes, D.Y. Cong, Z.H. Nie, Y. Ren, Y.D. Wang, Outstanding caloric performances for energy-efficient multicaloric cooling in a Ni-Mn-based multifunctional alloy, Acta Mater. 177 (2019) 46-55.

[66] S.L. Liu, H.C. Xuan, T. Cao, L.B. Wang, Z.G. Xie, X.H. Liang, H. Li, L. Feng, F.H. Chen, P.D. Han, Magnetocaloric and elastocaloric effects in all-d-metal $Ni_{37}Co_9Fe_4Mn_{35}Ti_{15}$ magnetic shape memory alloy, Phys. Status Solidi A 216 (2019) 1900563.

[67] T. Cao, H.C. Xuan, S.L. Liu, L.B. Wang, Z.G. Xie, X.H. Liang, F.H. Chen, P.D. Han, D.H. Wang, Y.W. Du, Enhanced elastocaloric effect and mechanical properties of Fe-doped Ni-Mn-Al ferromagnetic shape memory alloys, Intermetallics 112 (2019) 106529.

[68] A. Shen, D.W. Zhao, W. Sun, J. Liu, C.J. Li, Elastocaloric effect in a $Co_{50}Ni_{20}Ga_{30}$ single crystal, Scr. Mater. 127 (2017) 1-5.

[69] Y. Xu, B.F. Lu, W. Sun, A. Yan, J. Liu, Large and reversible elastocaloric effect in dual-phase $Ni_{54}Fe_{19}Ga_{27}$ superelastic alloys, Appl. Phys. Lett. 106 (2015) 201903.

[70] M. Imran, X.X. Zhang, M.F. Qian, L. Geng, Enhancing the elastocaloric cooling stability of Ni-Fe-Ga alloys via introducing pores, Adv. Eng. Mater. 22 (2020) 1901140.

[71] M. Imran, X.X. Zhang, Elastocaloric effects in polycrystalline Ni-Fe-Ga foams with hierarchical pore architecture, Phys. Rev. Mater. 4 (2020) 065403.

[72] Y. Wu, E. Ertekin, H. Sehitoglu, Elastocaloric cooling capacity of shape memory alloys–Role of deformation temperatures, mechanical cycling, stress hysteresis and inhomogeneity of transformation, Acta Mater. 135 (2017) 158-176.

[73] Y. Li, D.W. Zhao, J. Liu, S.X. Qian, Z.B. Li, W.M. Gan, X. Chen, Energy-efficient elastocaloric cooling by flexibly and reversibly transferring interface in magnetic shape-memory alloys, ACS Appl. Mater. Interfaces 10 (2018) 25438-25445.

[74] X.M. Huang, Y. Zhao, H.L. Yan, N. Jia, B. Yang, Z.B. Li, Y.D. Zhang, C. Esling, X. Zhao, Q.Y. Ren, X. Tong, L. Zuo, Enhanced cyclic stability and enlarged working temperature window of NiFeGa elastocaloric refrigerant via introducing strong texture and ductile interfacial precipitate, Scr. Mater. 234 (2023) 115544.

[75] C. Liu, Y.P. Wang, H.Q. Du, Z.B. Li, H.L. Yan, B. Yang, L. Zuo, Giant mechanical energy storage capacity and long-term mechanical cyclability in a fine-grained Heusler-type $Co_{51}V_{33}Ga_{16}$ shape memory alloy, Acta Mater. 277 (2024) 120185.

[76] P.L. Swanson, C.J. Fairbanks, B.R. Lawn, Y.W. Mai, B.J. Hockey, Crack-interface grain bridging as a fracture resistance mechanism in ceramics: I, experimental study on Alumina, J. Am. Ceram. Soc. 70 (1987) 279-289.

[77] K.S. Chan, Intermetallic composites toughened with ductile reinforcements, Intermetallic Matrix Composites. Woodhead Publishing, (2018) 359-407.

[78] Q.H. Meng, T.J. Wang, An improved crack-bridging model for rigid particle-polymer composites, Eng. Fract. Mech. 211 (2019) 291-302.

[79] Y.T. Song, X. Chen, V. Dabade, T.W. Shield, R.D. James, Enhanced reversibility and unusual microstructure of a phase-transforming material, Nature 502 (2013) 85-88.

[80] J. Cui, Y.S. Chu, O.O. Famodu, Y. Furuya, J. Hattrick-Simpers, R.D. James, A. Ludwig, S. Thienhaus, M. Wuttig, Z.Y. Zhang, I. Takeuchi, Combinatorial search of thermoelastic shape-memory alloys with extremely small hysteresis width, Nat. Mater. 5 (2006) 286-290.

[81] R. Zarnetta, R. Takahashi, M.L. Young, A. Savan, Y. Furuya, S. Thienhaus, B. Maaß, M. Rahim, J. Frenzel, H. Brunken, Y.S. Chu, V. Srivastava, R.D. James, I. Takeuchi, G. Eggeler, A. Ludwig, Identification of quaternary shape memory alloys with near-zero thermal hysteresis and unprecedented functional stability, Adv. Funct. Mater. 20 (2010) 1917-1923.

[82] R.D. James, K.F. Hane, Martensitic transformations and shape-memory materials, Acta Mater. 48 (2000) 197-222.

[83] L. Caron, P. Devi, A.M.G. Carvalho, C. Felser, S. Singh, Minimizing hysteresis in martensite phase transforming magnetocaloric Heusler alloys, arXiv (2018) 1806.05075.

[84] D.Y. Cong, L. Huang, V. Hardy, D. Bourgault, X.M. Sun, Z.H. Nie, M.G. Wang, Y. Ren, P. Entel, Y.D. Wang, Low-field-actuated giant magnetocaloric effect and excellent mechanical properties in a NiMn-based multiferroic alloy, Acta Mater. 146 (2018) 142-151.